Individual lava flow thicknesses in oceanus procellarum and mare serenitatis determined from clementine multispectral data

Shoshana Z. Weider, Ian A. Crawford, Katherine H. Joy

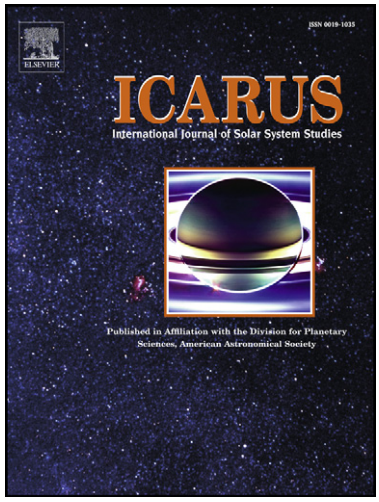

Individual lava flow thicknesses in oceanus procellarum and mare serenitatis determined from clementine multispectral data

Shoshana Z. Weider, Ian A. Crawford, Katherine H. Joy

PII: S0019-1035(10)00201-0
DOI: 10.1016/j.icarus.2010.05.010
Reference: YICAR 9431

To appear in: *Icarus*

Received Date: 16 March 2010
Revised Date: 13 May 2010
Accepted Date: 14 May 2010

Please cite this article as: Weider, S.Z., Crawford, I.A., Joy, K.H., Individual lava flow thicknesses in oceanus procellarum and mare serenitatis determined from clementine multispectral data, *Icarus* (2010), doi: 10.1016/j.icarus.2010.05.010

INDIVIDUAL LAVA FLOW THICKNESSES IN OCEANUS PROCELLARUM AND MARE SERENITATIS DETERMINED FROM CLEMENTINE MULTISPECTRAL DATA

Shoshana Z. Weider[a,b,c*], Ian A. Crawford[a,b], Katherine H. Joy[a,b,d,e]

[a] Department of Earth and Planetary Sciences, Birkbeck College, Malet Street, London, WC1E 7HX, UK.

[b] Centre for Planetary Sciences at UCL/Birkbeck, Gower Street, London, WC1E 6BT, UK.

[c] Space Science and Technology Department, Rutherford Appleton Laboratory, Didcot, Oxon, OX11 0QX, UK.

[d] Center for Lunar Science and Exploration, The Lunar and Planetary Institute, USRA, 3600 Bay Area Blvd, Houston, Texas 77058, USA.

[e] The NASA Lunar Science Institute.

KEYWORDS

Cratering; Moon, surface; spectroscopy; volcanism

ABSTRACT

We use multispectral reflectance data from the lunar Clementine mission to investigate the impact ejecta deposits of simple craters in two separate lunar mare basalt regions, one in Oceanus Procellarum and one in Mare Serenitatis. Over one hundred impact craters are studied, and for a number of these we observe differences between the TiO_2 (and FeO) contents of their ejecta deposits and the lava flow units in which they are located. We demonstrate that, in the majority of cases, these differences cannot plausibly be attributed to uncorrected maturity effects. These observations, coupled with morphometric crater relationships that provide maximum crater excavation depths, allow the investigation of sub-surface lava flow stratigraphy. We provide estimated average thicknesses for a number of lava flow units in the two study regions, ranging from ~80 m to ~600 m. In the case of the Serenitatis study area, our results are consistent with the presence of sub-surface horizons inferred from recent radar sounding measurements from the JAXA *Kaguya* spacecraft. The average lava flow thicknesses we obtain are used to make estimates

of the average flux of volcanic material in these regions. These are in broad agreement with previous studies, suggesting that the variation in mare basalt types we observe with depth is similar to the lateral variations identified at the surface.

1. Introduction

Mapping studies of the nearside lunar mare basalts have demonstrated that they are mosaics of temporally distinct lava flows (e.g. Wilhelms and McCauley 1971; Scott et al., 1977; Pieters 1978; Heather and Dunkin 2002; Hiesinger et al., 2003). These areas therefore potentially contain scientifically valuable localities for future human and/or robotic exploration (e.g. Spudis, 1996; Crawford et al., 2007; Fagents et al., 2010). The analysis of lunar rock samples, collected *in-situ* from distinct lava flows, would help solve some of the outstanding issues in lunar science, e.g.: (i) the volcanic history and evolution of the lunar mantle would be elucidated in greater detail by the study of samples from numerous, temporally distinct lava flows (e.g. Shearer et al., 2006); (ii) the calibration of the absolute lunar chronology and crater-counting curves would be improved by obtaining absolute radiometric ages for these lava flows (e.g. Stöffler et al., 2006) and; (iii) the study of the ancient Sun, and other early solar system conditions, could be achieved by sampling palaeoregolith material trapped between consecutive lava flows (e.g. Wieler et al., 1996; Crawford et al., 2007; Fagents et al., 2010). The scientific output from any future exploration within the mare basins would be maximised by choosing a landing site where a diverse array of geological units occurs within an accessible radius. Such sites may include contacts between two or more individual lava flow deposits, or material around impact craters that has been excavated during the impact event, and therefore negates the need for sub-surface drilling. In this paper impact craters within regions of two of the Moon's major nearside maria, Oceanus Procellarum and Mare Serenitatis, are studied with a view to identifying ejecta deposits that have excavated sub-surface lava flows that would otherwise be inaccessible.

1.1. Impact craters: windows through lava flows

During the formation of an impact crater, material from different vertical horizons within the original target surface is displaced or excavated. Material closest to the original surface acquires the most energy during the impact; it therefore has the greatest displacement and is deposited in

the continuous ejecta blanket that extends for about one crater radius beyond the crater rim (Moore et al., 1974; Oberbeck et al., 1974). Originally deeper material is re-deposited around the rim and interior of the resultant crater. Situations occur in the maria where feldspathic basement material (e.g. the primary lunar crust) is overlain by a stack of temporally and compositionally distinct lava flows (e.g. Hiesinger et al., 2003). Smaller impact craters within this region may have excavated through to underlying lava flows, which, providing the effects of space weathering can be accounted for, may remain identifiable in the ejecta surrounding the craters from orbital remote sensing measurements.

The NASA Clementine mission (Nozette et al., 1994) produced a global, high-spatial resolution (100 m/pixel) multispectral dataset suitable for studying local geological and compositional variations of this kind. Indeed, in an earlier study Heather and Dunkin (2002) used Clementine UV-Vis data to investigate impact craters in Oceanus Procellarum, and were able to distinguish anorthositic and basaltic material in a small proportion of the craters studied and from which they derived the total basalt thickness in this area. The aim of this work is to extend this approach to the identification of individual sub-surface lava flow layers with different compositions (as achieved by Rajmon and Spudis 2004, in Mare Tranquillitatis and Mare Fecunditatis).

1.2. FeO &TiO_2 abundance algorithms

Mare basalt hand specimens are usually classified primarily by their bulk rock TiO_2 contents (Neal and Taylor 1992) which can vary from <1 wt. % to ~13 wt. % (e.g. BVSP 1981; Taylor et al., 1991). As such, lateral and vertical compositional variations of lava flows in the mare regions can also be classified on this basis from remote sensing data sensitive to TiO_2 concentration. The relationships between lunar surface reflectance spectra and sample FeO and TiO_2 contents have led to the development of several quantitative methods for estimating the composition of the lunar surface (in terms of these oxides) from suitable remote sensing datasets.

An increase in the amount of iron contained within mafic silicate minerals causes a decrease in their albedo and a strengthening of their 1 μm absorption bands (e.g. Pieters 1993). There is also a corresponding decrease in the ratio between the near infra-red and visible wavelengths (NIR/Vis) (Burns 1993). However, these compositional relationships are affected by space weathering

97 effects. Space weathering is the process by which the lunar surface is physically and chemically
98 altered due to its continual bombardment by cosmic rays, solar wind particles and
99 micrometeorites, as well as the subsequent formation of new phases including single-domain
100 nanophase iron, agglutinates (impact-glass welded conglomerates of regolith particles) and
101 amorphous coatings on individual grains (Hapke et al., 1975; McKay et al., 1974, 1991; Morris
102 1976; Borg et al., 1980; Keller and McKay 1993; Fischer and Pieters 1994; 1996). These effects
103 cause a decrease in reflectance and a concomitant increase in the NIR/Vis (950/750 nm)
104 reflectance ratio (e.g. Fischer and Pieters 1994). The opposing effects of space weathering (so-
105 called 'maturity') and iron-silicate abundance on the reflectance spectra must therefore be
106 effectively decoupled in order to make reliable quantitative estimates of surface ferrous iron
107 content. Several such methods have been proposed (e.g. Lucey et al., 1995; Le Mouélic et al.,
108 2000; Lucey et al., 2000; Gillis et al., 2004; Wilcox et al., 2005).
109
110 In this work we employ the algorithm of Wilcox et al. (2005) because it most reliably removes the
111 effects of space weathering from mare reflectance spectra. This method makes use of the
112 relationship between the reflectance in the 750 nm waveband and the 950/750 nm reflectance ratio
113 from Clementine data of different mare materials. Staid and Pieters (2000) suggested that the
114 trends of samples with different ferrous iron concentrations were parallel on a plot of 750 nm
115 reflectance against the 950/750 nm ratio. It had previously been thought that these trends were
116 more radial in nature and this assumption had been employed in the algorithms of Lucey et al.
117 (1995; 2000) and Gillis et al. (2004). Wilcox et al. (2005) agree that a parallel model is more
118 accurate and thus use this observation in the formulation of their algorithm. Variations of
119 >0.5 wt. % in the deduced FeO concentration are thought to be due to true iron variations, rather
120 than incomplete suppression of maturity effects (Wilcox et al., 2005). A complementary means of
121 quantifying the degree of maturity of mare lunar soils is the mOMAT (mare Optical MATurity)
122 parameter of Wilcox et al. (2005). This numerical parameter varies between -1.05, for the most
123 mature materials, and -0.65 for the least mature (Wilcox et al., 2005).
124
125 The FeO abundance algorithm proposed by Le Mouélic et al. (2000) utilises reflectance values
126 from wavelengths in both the Clementine UV-Vis and NIR datasets (750, 950 and 1500 nm).
127 These are employed as band ratios only, and so this algorithm is less sensitive to the topographic
128 shading effects that plague the other methods (Lucy et al., 2000; Gillis et al., 2004; Wilcox et al.,

2005). However, large slopes (e.g. on crater walls) are unlikely to be a problem in this study because only areas that are generally flat are investigated (i.e. mare surfaces and ejecta blankets of small impact craters), and therefore the Wilcox et al. (2005) FeO algorithm was employed.

Similar methods for estimating the TiO_2 abundance of lunar soils have also been developed (e.g. Lucey et al., 1996; 2000; Gillis et al., 2003), based on a correlation between the TiO_2 content and the UV-Vis ratio of mature lunar soils (e.g. Charette et al., 1974; Johnson et al., 1991; Melendrez et al., 1994). The Lucey et al. (2000) algorithm uses the 750 nm waveband and the 415/750 nm ratio of Clementine reflectance values to define this relationship, and is utilised in this study because it is optimised to remove the effects of space weathering. Although it has a quoted estimated 1 σ error of 1 wt. %, later studies have cast doubts over its ability to accurately determine the true TiO_2 concentration of the lunar surface (Gillis et al., 2003; Gillis-Davis et al., 2006), and so the actual error may be somewhat larger. However, for this particular study, obtaining the absolute abundance of TiO_2 was less critical than ensuring that the differences in maturity of separate regions were properly accounted for and that their *relative* differences in TiO_2 content are significant.

2. This study

The large compositional diversity of lava flows in Oceanus Procellarum (Hiesinger et al., 2003) provides a suitable area to test the method of employing impact craters to probe subsurface lava flow stratigraphy. The area chosen for study here contains a significant number of individual lava flows within close proximity. Some regions of Mare Serenitatis are also of interest, as the sub-surface structure there has previously been investigated using *Kaguya* radar data (Ono et al., 2009). The method proposed here may therefore be used to independently check their conclusions.

For this study we downloaded Clementine UV-Vis multispectral data for the two separate regions (Oceanus Procellarum: 0° – 15°N; 300° – 315°W, and Mare Serenitatis: 16° – 33°N; 20° – 26°E) at full resolution (0.1 km/pixel) and in a simple cylindrical projection from the USGS Map-A-Planet website (www.mapaplanet.com) as radiometrically, geometrically and photometrically controlled .raw files (Eliason et al., 1999). These files were extracted and analysed using an in-

house IDL (Interactive Data Language) code in order to map the areas in terms of their FeO and TiO_2 contents according to the algorithms of Wilcox et al. (2005) and Lucey et al. (2000) respectively. The lava flow boundaries are defined as those mapped by Hiesinger et al. (2003) for the Oceanus Procellarum region and by Hiesinger et al. (2000) for the Mare Serenitatis region. Albedo images (Clementine 750 nm) of the two regions are shown in Figures 1 and 2 (where individual lava flows are identified according to the nomenclature of Hiesinger et al., 2000; 2003). Mean impact crater ejecta compositions are derived from the sampling of multiple (typically 10 – 30; see Table 1 and 2 for the precise number) pixels within the continuous ejecta blankets of these craters, which are assumed to extend for one crater radius beyond the rim (Moore et al., 1974; Oberbeck et al., 1974), even when an ejecta blanket is not discernable or is observed to extend further. The average composition of the continuous ejecta will be a mixture of all excavated layers, including the surface in which the crater formed. Mean lava flow FeO and TiO_2 values are similarly derived from multiple (>100; see Table 1 and 2 for the exact number) pixels within the inter-crater areas of the deposits.

3. Results

3.1. Study Area 1: Marius Region (0° – 15°N; 300° – 315°W), Oceanus Procellarum

The TiO_2 concentration map of this area reveals a number of craters within a particular lava flow unit (flow 'P52' of Hiesinger et al., 2003, immediately to the east of Marius Hills) that appear to be surrounded by haloes of material with a lower TiO_2 content than the surrounding lava flow, and which approximate the extent of their continuous ejecta blankets. These craters are circled and numbered (1 to 13) in Figure 3, which shows a small subset of the area (a set of 18 craters with no discernable haloes are also shown and labelled 'A' – 'S' in Figure 3). We hypothesise that these haloes evidence material with a lower TiO_2 abundance that has been excavated from a lithology beneath the surface flow ('P52'). A candidate for this lithology is the stratigraphically lower lava flow 'P24', which is TiO_2-poorer (by ~3 wt. %).

Figure 4 is a plot of mean FeO and TiO_2 wt. % abundances for (i) the ejecta of the thirteen craters with TiO_2-poor haloes identified in lava flow unit 'P52' and (ii) the mean lava flow compositions for 'P52' and 'P24'. It illustrates that the ejecta of the thirteen haloed craters have a distinct

192 composition from that of lava flow 'P52' in which they are located, and that the ejecta
193 compositions are more similar to that of the proposed underlying unit, 'P24'.
194
195 The increase in nanophase iron in lunar soils due to space weathering causes a darkening of
196 reflectance spectra, as does increased abundance of ilmenite (the major TiO_2 bearing opaque phase
197 in lunar soils). It is therefore important to confirm that the apparent lower TiO_2 content of these
198 crater ejecta is due to an actual compositional difference compared to the lava flow unit in which
199 they are located, rather than to an unresolved maturity (albedo) issue. We believe that these TiO_2-
200 poor haloes are indeed evidence of a true compositional difference for a number of reasons
201 illustrated in Figure 5:
202
203 (i) On a plot of the 415/750 nm reflectance ratio versus albedo (750 nm), the ejecta of the haloed
204 craters in lava flow 'P52' form a distinct group from the ejecta of a set of craters with no haloes in
205 the same lava flow (Figure 5a); the offset of these two groups follows a trend of increased TiO_2
206 content rather than one of increased maturity;
207
208 (ii) The majority of the craters (both with and without TiO_2-poor haloes) have a similar, narrow
209 range of mature mOMAT values (Figure 5b), indicating that the sampled craters all have a similar
210 level of maturity; and
211
212 (iii) As a function of crater diameter, the two sets of craters display a clear distinction in
213 TiO_2 wt. % values, but not in albedo (Figure 5c, d).
214
215 Given that the identified craters with TiO_2-poor haloes in lava flow 'P52' have indeed excavated
216 material from a deeper, compositionally different lava flow (i.e. 'P24'), their diameters can be
217 used to estimate their maximum depth of excavation and therefore constrain the thickness of the
218 surficial lava flow ('P52'). The maximum excavation depth (D_{exc}) of simple craters (i.e. those
219 with diameters < 15 km) can be calculated using the following equation (Melosh 1989):
220 $D_{exc} = 0.1 \times D_t$, where D_t is the transient cavity diameter. The transient cavity diameter is defined
221 by Melosh (1989) as: $D_t = 0.84 \times D$ (where D is the present, rim-rim diameter of the crater).
222 These values are listed in Table 1.
223

The maximum excavation depths of the TiO_2-poor haloed craters are used to provide an upper bound for the thickness of unit 'P52' where it overlies 'P24' in this area, whereas the excavation depths of the non-haloed craters provide a lower limit for this thickness. The maximum excavation depth estimates (in km) for the craters with and without TiO_2-poor haloes in lava flow 'P52' are shown in Figure 6. The results show that 'P24' is between ~100 m and 300 m below the surface of 'P52' in the area that has been investigated.

The total thickness of the mare basalt deposit within Oceanus Procellarum has previously been estimated using a variety of techniques. Morphometric crater relationships (Pike 1974; 1977) and the heights of exposed rims were used to infer the burial depths of partially buried craters (De Hon 1978; 1979). The isopach map produced by De Hon (1979) gives a total basalt thickness estimate in this study area of 500 to 1000 m. Craters which have excavated basement anorthositic material have been used to estimate the total thickness of the overlying basalt (Heather and Dunkin 2002), and are in broad agreement with the earlier study by De Hon (1979). The new results presented here extend this approach by providing an estimate of the thickness of individual lava flows within a stack of temporally and compositionally distinct deposits. If 'P52' (with an estimated thickness of ~100 to 300 m) constitutes about half of the minimum estimated (i.e. 500 m) total depth of basaltic material in this region, then we predict that 'P24' has a similar thickness and completes the basin fill. However, if there is an additional, un-sampled flow(s) underlying 'P24', its true thickness would be smaller.

3.2. Study Area 2: Central Southern Mare Serenitatis (16° – 33°N; 20° – 26°E)

We have also used Clementine multispectral reflectance data to investigate the lava flow stratigraphy of an area in Mare Serenitatis (Figure 2). It was chosen because it coincides with published *Kaguya* radar tracks (Ono et al., 2009) that were used to infer the depth of a specific lava flow unit beneath the surface. The TiO_2 abundance of the separate lava flow units in this area (whose boundaries and names are taken from Hiesinger et al., 2000) vary significantly, from very low-Ti basalts in the northwest, to high-Ti basalts in the southeast (see Figure 7). A total of 103 (simple) impact craters throughout the region were selected and their continuous ejecta blankets sampled in order to search for evidence of their excavating compositionally distinct material from beneath the surface.

Mean FeO and TiO_2 wt. % content values for the inter-crater areas of the eight lava flow units are shown in Figure 8. Although the difference in the composition of the southern units 'S11' and 'S18' compared to the more northern flows is clear, some of the units identified by Hiesinger et al. (2000) are indistinguishable based on this classification, which is not surprising because the earlier study used morphological features in addition to compositional differences to map the lava flow boundaries. Figure 9 shows a series of FeO vs. TiO_2 plots for each of the lava flow units that contain the craters sampled in this investigation, displaying the mean flow values as well as those for the craters within each particular unit. Details of individual craters studied are given in Table 2 and the estimated absolute ages (Hiesinger et al. 2000) of the lava flows in Table 3.

For the Oceanus Procellarum study (Section 3.1) it was important to determine if the apparently TiO_2-poor ejecta haloes around selected impact craters was due to true compositional variations or unresolved maturity issues. For the craters in Mare Serenitatis, this issue is less important because most of the craters with compositionally anomalous ejecta appear to have excavated material richer in TiO_2 rather than poorer, and so the trends of maturity and composition are in opposition. The mOMAT (Wilcox et al., 2005) values of all 103 sampled craters are given in Table 2 and shown in Figure 10; the vast majority fall within a narrow band of mature values, with only three craters (75, 87 and 101) being more immature and fresh. Maximum excavation depths for these latter three craters are therefore ignored in making lava flow thickness estimates.

In the following sections we discuss the results obtained for the various lava flow units (where the lava flow nomenclature is that of Hiesinger et al., 2000).

3.2.1 Lava flow 'S13'

In terms of FeO and TiO_2 content, the ejecta compositions of the seven craters sampled in the small corner of 'S13' (Figure 9a) do not differ significantly from the lava flow itself. The crater diameters and their associated excavation depths therefore provide a lower bound for the thickness of 'S13' in this area; crater 6 is the largest and constrains the thickness of the unit to > 585 m.

3.2.2 Lava flow 'S15'

Two craters in this unit (87 and 101) have higher mOMAT values (see Figure 10) than the vast majority of the 103 craters sampled within Mare Serenitatis (the freshness of crater 101 can explain its apparently low FeO and TiO_2 content; Figure 9b); these two craters were therefore not used in making lava flow thickness interpretations. For the other craters measured in 'S15', the ejecta compositions generally match that of the flow itself (Figure 9b). However, there is a subset that appears to have excavated older, compositionally distinct lithologies. Crater 41 seems to have excavated material from the underlying lava flow 'S13', and can therefore provide a thickness estimate of <120 m for 'S15' in the immediately surrounding area. Craters 42 and 43 are two smaller craters just to the south of crater 41 and they do not appear to have excavated the same material as it. The diameters of all three craters (41, 42, and 43) can therefore be used to constrain the 'S15' thickness estimate to between ~50 and ~120 m. Craters 84, 85 and 91 also appear to have excavated a separate unit underlying 'S15' that possesses a higher content of both FeO and TiO_2. Although on the basis of Figure 9b it would seem that 'S22' is a candidate for the excavated unit, this cannot be the case if the ages determined by Hiesinger et al. (2000) are correct and 'S22' is indeed *younger* than 'S15'. It is possible that these four craters have instead excavated a unit with a similar FeO and TiO_2 content to 'S22', but which has no surface expression in this area; or that they have excavated 'S11' and that the average compositions of their ejecta represent a level of mixing between this older flow, which is richer in FeO and TiO_2, and 'S15' itself. These craters can still be used to constrain the thickness of 'S15' where it overlies such a lava flow to < ~225 m. In addition, the size of the craters in 'S15' whose ejecta lack any compositional anomalies, indicate that there is considerable variability in the thickness of 'S15' over the study area.

3.2.3 Lava flow 'S16'

Only two craters were sampled from 'S16', however a difference between their ejecta compositions is noted (Figure 9c). The composition of the ejecta from crater 102 resembles that of 'S16', whereas that from crater 103 has a higher content of both FeO and TiO_2. As for unit 'S15', it is not possible for crater 103 to have excavated material from the younger units 'S18', 'S22', 'S24' or 'S28' and so there is the potential for craters 103 (in 'S16') and 84, 85 and 91 (in 'S15') to have all sampled either an unidentified underlying unit, or 'S11'. In the case of 'S11' having been excavated, the ejecta composition of crater 103 would represent a mixture of 'S16' and the

older, more FeO and TiO_2-rich flow. Using the diameters of the craters 102 and 103, the thickness of this part of lava flow unit 'S16' is estimated to be between ~65 and ~100 m.

3.2.4 Lava flow 'S22'

All of the nine craters sampled within lava flow unit 'S22' have ejecta that match the composition of the unit itself (Figure 9d). As such, they provide only a lower bound for the thickness of 'S22'; it is estimated to be at least ~100 m thick in this region.

3.2.5 Lava flow 'S24'

The ejecta of the five craters sampled in 'S24' (Figure 9e) have slightly elevated TiO_2 contents compared to that of the lava flow itself, suggesting that material from an older lithology such as 'S22', or the unidentified unit potentially sampled by craters in 'S15' and 'S16', has been excavated. Given the position of 'S24' next to units 'S15' and 'S16' and removed from 'S22', the second option is perhaps more likely. It is also possible that the craters in 'S24' have ejecta compositions that are mixtures of the surface lava flow and an older lava flow such as 'S11' or 'S18'. If this set of craters has indeed excavated material from a separate lava flow, the thickness of 'S24' above it can be constrained to < ~125 m.

3.2.6 Lava flow 'S28'

Crater 75, within lava flow unit 'S28' (Figure 9f) has a higher mOMAT value than the majority of the craters sampled in this study (Figure 10) and therefore is disregarded in estimating the thickness of 'S28'. Craters 9 and 45, in the north of 'S28' appear to have excavated material from the neighbouring unit, 'S15'. Their sizes, along with that of nearby crater 46, are used to constrain the thickness of 'S28' where it overlies 'S15' in this region to between ~120 and ~290 m. About half of the craters in 'S28' have ejecta with a distinct composition to that of the lava flow, and appear to have excavated material from a unit with higher FeO and TiO_2 contents, such as 'S11'. 'S18 or 'S22'. Craters 61, 63 and 64 all have ejecta with compositions different to 'S28', whereas neighbouring craters 60, 62, 90 and 89 do not. The thickness of 'S28' is thus estimated to be between ~40 and ~100 m where it overlies 'S22' (or a similarly FeO and TiO_2 enriched lava flow

352 in this region). Craters 89 and 90 do not have compositionally anomalous haloes, and are larger
353 than the three craters that do, possibly indicating local variations in the surface unit thickness that
354 may be caused by the underlying topography. A large number of craters within the southernmost
355 third of 'S28' have compositionally anomalous ejecta deposits and appear to have excavated
356 material from lava flow 'S22' (or perhaps 'S11' / 'S18'). There are considerable variations in the
357 depth estimates provided by these craters that are probably due to local topographical changes, but
358 for a small area around craters 23 – 27, for example, the thickness of 'S28' is estimated at ~80 m.
359
360 A summary of these findings is illustrated in the map shown in Figure 11. All 103 craters are
361 shown and those that are noteworthy are labelled with their number. Those craters whose ejecta
362 have excavated a sub-surface lithology are represented by circles of the colour corresponding to
363 the lava flow from which it is proposed the material originated; black circles mark craters without
364 compositional anomalies. The three yellow circles represent the craters with immature mOMAT
365 values. Figure 12a shows the estimated maximum excavation depths (in metres) for all the
366 sampled impact craters (other than the three with high mOMAT values); Figure 12b shows
367 approximate thickness estimates (in metres) for the surface flows we have made based on these
368 excavation depth constraints.
369
370 *3.2.7. Comparisons with other studies*
371
372 The Lunar Radar Sounder (LRS) on the Japanese Kaguya spacecraft was a high-frequency
373 imaging radar instrument, which allowed the lunar subsurface stratigraphy and tectonic features to
374 be probed, with global coverage (Ono et al., 2009; Pommerol et al., 2010). The 5 MHz frequency
375 permitted subsurface data to be obtained to a depth of several kilometres (Ono et al., 2009), with
376 an estimated vertical resolution ranging between 25 and 40 m (Pommerol et al., 2010). This
377 technique specifically detects differences in the dielectric constant of the subsurface materials,
378 which is affected on the Moon by factors such as porosity and composition.
379
380 On the basis of Kaguya LRS data, Ono et al. (2009) observe a sub-surface reflector at a depth of
381 ~175 m at point A (20°N, 23.3°E) in Figure 12b. They interpret this reflector as a high porosity
382 deposit (buried regolith rather than a pyroclastic deposit or ejecta deposits) on the top of unit 'S11'
383 which they can trace to where it outcrops at the surface. This interpretation is possibly in

agreement with our new estimates if 'S22' lies between the surface flow 'S28' and the reflector which marks the top of 'S11'. The craters in 'S28' which appear to have excavated material from 'S22' constrain the thickness of 'S28' at this point to ~ 75 m. 'S22' must therefore be ~ 100 m thick at this point. This fits well with the constraints provided by the craters in 'S22' that do not excavate a deeper lithology. Ono et al. (2009) do not observe a sub-surface boundary corresponding to the top of 'S22', but this may be because such a boundary at a depth of only 75 m is below their resolution. The deeper 'S11' boundary may also be more pronounced than for 'S22' because of its greater TiO_2 content (Pommerol et al., 2010). Ono et al. (2009) also identify the top of 'S11' at a similar depth (~ 175 m) beneath 'S15' at point B (19°N, 25.5°E) in Figure 12b. The craters in this part of 'S15' suggest that an older lava flow does exist at around this depth, but the composition of the ejecta do not obviously indicate that it is 'S11'. These ejecta do have higher TiO_2 (and FeO) contents than that of 'S15', but they do not appear to match any of the lava flow units currently exposed at the surface in Mare Serenitatis. These compositions could therefore represent an additional sub-surface lava flow (the top of which has been imaged by Ono et al. (2009) and misidentified by them as 'S11'), or be due to mixing between the high FeO and TiO_2 contents of 'S11' and the surface lava flow 'S15' in the crater ejecta blankets.

The total thickness of mare fill within the Serenitatis basin has previously been estimated to be ~ 4 km (Williams and Zuber 1998, although larger (~8.5 km; Solomon and Head 1980) and smaller (~3.5 km; De Hon 1974; 1979; De Hon and Waskom 1976) estimates have also been made. The surface lava flows whose thicknesses have been estimated in this study therefore contribute only a fraction of the total mare fill.

4. Discussion

It is important to understand the thickness of the mare basalts, and the individual lava flow units of which they consist, so that the total volume of volcanic material at the lunar surface can be determined. This allows the evolution of the lunar interior to be investigated, for example the extent of partial melting of the mantle with time.

Table 4 shows estimated (and approximate) values for various parameters relating to the lava flow units studied in both Oceanus Procellarum and Mare Serenitatis. Using the estimated average

thickness of the flows, for which this has been determined, and their surface area (Hiesinger et al., 2000; 2003), an approximate minimum volume for the units can be determined. A maximum time interval within which the individual flows were emplaced can be constrained from the difference in absolute ages of the flow in question and the unit immediately older than it in the stratigraphy (Hiesinger et al., 2000; 2003). This enables an average 'flux' of magma eruption to be calculated. Of course, the actual length of time over which these flows erupted would have been essentially instantaneous on these timescales, so the flux derived here is purely a measure of the amount of material that reached the surface within each several hundred million year interval. Even for these gross averages there are several caveats: (i) the apparent (absolute) age dating of the lava flow units by crater counting inherently involves large errors; (ii) extrapolation of the thickness of a whole lava flow from only a few spot estimates may be problematic; (iii) the area of the surface flows, and especially the older flows, as given by (Hiesinger et al., 2000; 2003) are likely to be underestimated due to coverage by subsequent flows and; (iv) the TiO_2 abundances upon which our thickness estimates are based, are estimated from an algorithm (Lucey et al., 2000) which has a 1 σ error of at least 1 wt. %. Although this algorithm may over or underestimate the true TiO_2 wt. % content of the regolith by up to ~5 wt. % in some areas (Gillis et al., 2003), it is the *relative* difference between the values from different deposits that is important in this study, as well as the suppression of any maturity effects.

Knowledge of the flux of lunar volcanism can help refine the understanding of mare basalt petrogenesis and the relationship between the basalts and the Moon's magmatic and thermal evolution (e.g. Head and Wilson 1992; Zhong et al., 1999; Parmentier 2000; Wieczorek and Phillips 2000; Wilson and Head 2001; Shearer et al., 2006). The precise shape of the lunar mare basalt flux curve is still uncertain; different shapes are derived from various methods (see discussion in Head and Wilson 1992). The determination of individual lava flow thicknesses and fluxes in different lunar maria would improve the overall accuracy to which this curve is known (Hiesinger et al., 2003).

Figure 13a illustrates the estimated flux for the lava flow units in this study (from Oceanus Procellarum and Mare Serenitatis) as a function of their crater-count age. Although the number of points in our dataset is quite small (Table 4), the overall shape of the curve produced is similar to the generalised mare basalt flux of Head & Wilson (1992), which is based on a combination of

448 approaches (e.g. data from returned samples and remote sensing) and superimposed for
449 comparison in Figure 13a.
450
451 Giguere et al. (2000) investigated the apparent dichotomy between the bimodal distribution of
452 lunar basalts in terms of TiO_2 content according to sample data, and the more unimodal
453 distribution suggested by remote sensing data. They concluded that of the mare basalts, the low-Ti
454 basalts are the most spatially abundant. If the flux of the lava flow units presented here is used as
455 a proxy for their total abundance, then the trend observed in Figure 13b can be compared to the
456 work of Giguere et al. (2000), with which it appears to agree. Figure 13b shows that the flux of
457 the low-Ti basalt units tends to be greater than that of the high-Ti units, i.e. the vertical variation in
458 the abundance of different basalt types shown here is similar to the lateral (surface) variation
459 previously identified.
460
461 **5. Conclusions**
462
463 Clementine UV-Vis reflectance data have been used to estimate the FeO and TiO_2 contents of
464 impact crater ejecta in two study areas (in Oceanus Procellarum and Mare Serenitatis). This
465 information has led to the identification of crater populations which have excavated material from
466 deeper, compositionally distinct lava flows. The depth-diameter relationship of simple craters
467 allows some constraints to be placed on the thickness of the surface units. Being able to constrain
468 the depth of lava flows in this way allows the volcanic history of the area to be better understood,
469 and by extrapolation allows lava flow volumes and fluxes to be estimated. This information in
470 turn allows a more detailed view of spatial and temporal variations in the thermal history of the
471 Moon.
472
473 The results presented are in broad agreement with previous work on lava flow thicknesses, and
474 with recent radar sounding results. It would therefore be of value to extend this method to wider
475 areas of the maria, and to employ newer, higher quality datasets. Data from the Spectral Profiler
476 (SP) onboard *Kaguya* (500 m spatial footprint; 296 spectral channels covering wavelengths
477 between 0.5 and 2.6 μm; Matsunaga et al., 2008), and the Moon Mineralogy Mapper (M^3) onboard
478 Chandrayaan-1 (80 m spatial footprint; up to 260 spectral channels covering wavelengths between
479 0.42 and 3.0 μm; Pieters et al., 2009), will be especially valuable in this respect.

6. Acknowledgments

We would like to thank Miriam Riner and David Rajmon for helpful reviews. S.Z.W. thanks the UK Science and Technology Facilities Council (STFC) for the award of a post-graduate studentship. I.A.C. and K.H.J. thank the Leverhulme Trust for financial support. This is LPI contribution number 1557.

References

Basaltic Volcanism Study Project, 1981. *Basaltic volcanism on the terrestrial planets*. Pergamon Press Inc, New York.

Borg, L.E., Shearer, C.K., Asmerom, Y. & Papike, J.J., 1980. Prolonged KREEP magmatism on the Moon indicated by the youngest dated lunar igneous rock, *Nature*, 432, 209-211.

Burns, R.G., 1993. *Mineralogical applications of crystal field theory*. Cambridge University Press.

Charette, M.P., McCord, T.B., Pieters, C. & Adams, J.B., 1974. Application of remote spectral reflectance measurements to lunar geology classification and determination of titanium content of lunar soils. *Journal of Geophysical Research*, 79 (11), 1605-1613.

Crawford, I.A., Fagents, S. & Joy, K.H., 2007. Full moon exploration – valuable (non-polar) lunar science facilitated by a return to the moon. *Astronomy and Geophysics*, 48 (3), 18-21.

De Hon, R.A., 1974. Thickness of mare material in the Tranquillitatis and Nectaris basins, *Proceedings of 5th Lunar Science Conference*, 53-59.

De Hon, R.A., 1978. Maximum thickness of materials in the western mare basins. *Proceedings of 9th Lunar and Planetary Science Conference*, 229-231.

512 De Hon, R.A., 1979. Thickness of the western mare basalts, *Proceedings of 10th Lunar and*
513 *Planetary Science Conference*, 2935-2955.
514
515 De Hon, R.A. & Waskom, J.D., 1976. Geologic structure of the eastern mare basins. *Proceedings*
516 *of 7th Lunar Science Conference*, 2729-2746.
517
518 Eliason, E., Isbell, C., Lee, E., Becker, T., Gaddis, L., McEwen, A. & Robinson, M., 1999. The
519 Clementine UVVIS global lunar mosaic. *NASA Planetary Data System CD-ROM Archive*, CL-
520 4001-4078.
521
522 Fagents, S.A., Rumpf, M.E., Crawford, I.A. & Joy, K.H., 2010. Preservation potential of
523 implanted solar wind volatiles in lunar palaeoregolith deposits buried by lava flows. *Icarus*, 207,
524 595-604.
525
526 Fischer, E.M. & Pieters, C.M., 1994. Remote determination of exposure degree and iron
527 concentration of lunar soils using VIS-NIR spectroscopic methods. *Icarus*, 111, 475-488.
528
529 Fischer, E.M. & Pieters, C.M., 1996. Composition and exposure age of the Apollo 16 Cayley and
530 Descartes regions from Clementine data: normalizing the optical effects of space weathering.
531 *Journal of Geophysical Research*, 101, 2225-2234.
532
533 Giguere, T.A., Taylor, G.J., Hawke, B.R. & Lucey, P.G., 2000. The titanium contents of lunar
534 mare basalts. *Meteoritics and Planetary Science*, **35**, 193-200.
535
536 Gillis, J.J., Jolliff, B.L. & Elphic, R.C., 2003. A revised algorithm for calculating TiO_2 from
537 Clementine UVVIS data: a synthesis of rock, soil, and remotely sensed TiO_2 concentrations.
538 *Journal of Geophysical Research*, 108 (E2), doi: 10.1029/2001JE001515.
539
540 Gillis, J.J., Jolliff, B.L. & Korotev, R. L., 2004. Lunar surface geochemistry: global
541 concentrations of Th, K, and FeO as derived from lunar prospector and Clementine data.
542 *Geochimica et Cosmochimica Acta*, 68 (18), 3791-3805.
543

544 Gillis-Davis, J.J., Lucey, P.G. & Hawke, B.R., 2006. Testing the relation between UV-vis color
545 and TiO_2 content of the lunar maria. *Geochimica et Cosmochimica Acta*, 70, 6079-6102.
546
547 Hapke, B., Cassidy, W. & Wells, E., 1975. Effects of vapor-phase deposition processes on the
548 optical, chemical, and magnetic properties of the lunar regolith. *The Moon*, 13, 339-353.
549
550 Head, J.W., III & Wilson, L., 1992. Lunar mare volcanism: stratigraphy, eruption conditions, and
551 the evolution of secondary crusts. *Geochimica et Cosmochimica Acta*, 56, 2155-2175.
552
553 Heather, D.J. & Dunkin, S.K., 2002. A stratigraphic study of southern Oceanus Procellarum using
554 Clementine multispectral data. *Planetary and Space Science*, 50, 1299-1309.
555
556 Hiesinger, H., Jaumann, R., Neukum, G. & Head, J.W., III, 2000. Ages of mare basalts on the
557 lunar nearside. *Journal of Geophysical Research*, 105 (E12), 29-239-29,275.
558
559 Hiesinger, H., Head, J.W., III, Wolf, U., Jaumann, R. & Neukum, G., 2003. Ages and stratigraphy
560 of mare basalts in Oceanus Procellarum, Mare Nubium, Mare Cognitum, and Mare Insularum.
561 *Journal of Geophysical Research*, 108 (E7), doi: 10.1029/2002JE001985.
562
563 Hood, L.L. & Williams, C.R., 1989. The lunar swirls: distribution and possible origins.
564 *Proceedings of 19th Lunar and Planetary Science Conference*, 99-113.
565
566 Johnson, J.R., Larson, S.M. & Singer, R.B., 1991. Remote sensing of potential lunar resources 1.
567 Near-side compositional properties. *Journal of Geophysical Research*, 96 (E3), 18,861-18,882.
568
569 Keller, L.P. & McKay, D.S., 1993. Discovery of vapour deposits in the lunar regolith. *Science*,
570 261, 1305-1307.
571
572 Le Mouélic, S., Langevin, Y., Erard, S., Pinet, P., Chevrel., S. & Daydou, Y., 2000.
573 Discrimination between maturity and composition of lunar soils from integrated Clementine UV-
574 visible/near-infrared data: application to the Aristarchus Plateau. *Journal of Geophysical*
575 *Research*, **105** (E4), 9445-9455.

Lucey, P.G., Blewett, D.T., Johnson, J.L., Taylor, G.J. & Hawke, B.R., 1996. Lunar titanium content from UV-VIS measurements. *Proceedings of 27th Lunar and Planetary Science Conference*, 781-782.

Lucey, P.G., Taylor, G.J. & Malaret, E., 1995. Abundance and distribution of iron on the Moon. *Science*, 268, 1150-1153.

Lucey, P.G., Blewett, D.T., & Jolliff, B.L., 2000. Lunar iron and titanium abundance algorithms based on final processing of Clementine ultraviolet-visible images. *Journal of Geophysical Research*, 105 (E8), 20,297-20,305.

Matsunaga, T., Ohtake, M., Haruyama, J., Ogawa, Y., Nakamura, R., Yokota, Y., Morota, T. Honda, C., Torii, M., Abe, M., Nimura, T., Hiroi, T., Arai, T., Saiki, K., Takeda, H., Hirata, N., Kodama, S., Sugihara, T., Demura, H., Asada, N., Terazono, J. & Otake, H., 2008. Discoveries on the lithology of lunar crater central peaks by SELENE Spectral Profiler. *Geophysical Research Letters*, 35, doi: 10.1029/2008GL035868.

McKay, D.S., Fruland, R.M. & Heiken, G.H., 1974. Grain size and the evolution of lunar soils. *Proceedings of 5th Lunar Science Conference*, 887-906.

McKay, D.S., Heiken, G., Basu, A., Blanford, G., Simon, S., Reedy, R., French, B.M. & Papike, J., 1991. The lunar regolith, in: Heiken, G.H., Vaniman, D.T. & French, B.M. (Eds), *Lunar sourcebook a user's guide*, Cambridge University Press, New York, 285-356.

Melendrez, D.E., Johnson, J.R., Larson, S.M. & Singer, R.B., 1994. Remote sensing of potential lunar resources 2. High spatial resolution mapping of spectral reflectance ratios and implications for nearside mare TiO_2 content. *Journal of Geophysical Research*, 99 (E3), 5601-5619.

Melosh, H.J., 1989. *Impact cratering - a geologic process*. Oxford University Press.

Morris, R.V., 1976. Surface exposure indices of lunar rocks: a comparative FMR study. *Proceedings of 7th Lunar Science Conference*, 315-335.

608

609 Moore, H.J., Hodges, C.A. & Scott, D.H., 1974. Multiringed basins – illustrated by Orientale and
610 associated features. *Proceedings of 5th Lunar Science Conference*, 1, 71-100.

611

612 Neal, C.R. & Taylor, L.A., 1992. Petrogenesis of mare basalts: a record of lunar volcanism.
613 *Geochimica et Cosmochimica Acta*, 56, 2177-2211.

614

615 Nozette, S. and the Clementine Team, 1994. The Clementine mission to the Moon: scientific
616 overview, *Science*, 266, 1835-1839.

617

618 Oberbeck, V.R., Morrison, R.H., Hörz, F., Quaide, W.L. & Gault, D.E., 1974. Smooth plains and
619 continuous deposits of craters and basins. *Proceedings of 5th Lunar Science Conference*, 1, 111-
620 136.

621

622 Ono, T., Kumamoto, A., Nakagawa, H., Yamaguchi, Y., Oshigami, S., Yamaji, A., Kobayashi, T.,
623 Kasahara, Y. & Oya, H., 2009. Lunar radar sounder observations of subsurface layers under the
624 nearside maria of the Moon. *Science*, 323, 909-912.

625

626 Parmentier, E.M., Zhong, S. & Zuber, M.T., 2000. On the relationship between chemical
627 differentiation and the origin of lunar asymmetries. *Proceedings of 31st Lunar and Planetary*
628 *Science Conference*, abstract #1614.

629

630 Pommerol, A., Kofman, W., Audouard, J., Grima, C., Beck, P., Mouginot, J., Herique, A.,
631 Kumamoto, A., Kobayashi, T., Ono, T., 2010. Detectability of subsurface interfaces in lunar maria
632 by the LRS/SELENE sounding radar: influence of mineralogical composition. *Geophysical*
633 *Research Letters*, 37, L03201, doi: 10.1029/2009GL041681.

634

635 Pieters, C.M., 1978. Mare basalt types on the front side of the Moon: a summary of spectral
636 reflectance data. *Proceedings of 9th Lunar and Planetary Science Conference*, 2825-2849.

637

638 Pieters, C.M., 1993. Lunar reflectance spectroscopy. In: Pieters, C.M. and Englert, P.A. (eds.),
639 *Topics in remote Sensing 4: Remote Geochemical Analysis -- Elemental and Mineralogical*
640 *Composition*, Cambridge University Press, Cambridge, pp. 309-339.
641
642 Pieters, C.M., Boardman, J., Buratti, B., Chatterjee, A., Clark, R., Glavich, T., Green, R., Head, J.,
643 III, Isaacson, P., Malaret, E., McCord, T., Mustard, J., Petro, N., Runyon, C., Staid, M., Sunshine,
644 J., Taylor, L., Tompkins, S., Varanasi, P. & White, M., 2009. The Moon Mineralogy Mapper (M^3)
645 on Chandrayaan-1. *Current Science*, 96 (4), 500-505.
646
647 Pike, R.J., 1974. Depth/diameter relations of fresh lunar craters: revision from spacecraft data.
648 *Geophysical Research Letters*, 1 (7), 291-294.
649
650 Pike, R.J., 1977. Size-dependence in the shape of fresh impact craters on the moon. In: *Impact*
651 *and explosion cratering: planetary and terrestrial implications; Proceedings of the Symposium on*
652 *Planetary Cratering Mechanics*, Pergamon Press, New York, 489-509.
653
654 Rajmon, D. & Spudis, P., 2004. Distribution and stratigraphy of basaltic units in Maria
655 Tranquillitatis and Fecunditatis: A Clementine perspective. *Meteoritics and Planetary Science*, 39
656 (10), 1699-1720.
657
658 Scott, D.H., McCauley, J.F. & West, M.N., 1977. Geologic map of the west side of the Moon.
659 *U.S. Geological Survey*, I-1034.
660
661 Shearer. C.K., Hess, P.C., Wieczorek, M.A., Pritchard, M.E., Parmentier, E.M., Borg, L.E.,
662 Longhi, J., Elkins-Tanton, L.T., Neal, C.R., Antonenko, I., Canup, R.M., Halliday, A.N., Grove,
663 T.L., Hager, B.H., Lee, D-C. & Wiechert, U., 2006. Thermal and magmatic evolution of the
664 Moon. *Reviews in Mineralogy and Geochemistry*, 60, 365-518.
665
666 Solomon, S.C. & Head, J.W., 1980. Lunar mascon basins: lava filling, tectonics, and evolution of
667 the lithosphere, *Reviews of Geophysics and Space Physics*, 18 (1), 107-141.
668
669 Spudis, P.D., 1996. *The once and future moon*. Smithsonian Institution Press, Washington.

Staid, M.I. & Pieters, C.M., 2000. Integrated spectral analysis of mare soils and craters: application to eastern nearside basalts. *Icarus*, 145, 122-139.

Stöffler D., Ryder G., Ivanov B. A., Artemieva N. A., Cintala M. J. and Grieve R. A. F., 2006. Cratering history and lunar chronology. *Reviews in Mineralogy and Geochemistry*, 60, 519-596.

Taylor, G.J., Warren, P., Ryder, G., Delano, J., Pieters, C. & Lofgren, G., 1991. Lunar rocks, in: Heiken, G.H., Vaniman, D.T. & French, B.M. (Eds), *Lunar sourcebook a user's guide*, Cambridge University Press, New York, 183-284.

Wieczorek, M.A. & Phillips, R.J., 2000. The "Procellarum KREEP Terrane": implications for mare volcanism and lunar evolution. *Journal of Geophysical Research*, 105 (E8), 20,417-20,430.

Wieler, R., Kehm, K., Meshik, A.P. & Hohenberg, C.M., 1996. Secular changes in the xenon and krypton abundances in the solar wind recorded in single lunar grains. *Nature*, 384, 46-49.

Wilcox, B.B., Lucey, P.G. & Gillis, J.J., 2005. Mapping iron in the lunar mare: an improved approach. *Journal of Geophysical Research*, 110, doi: 10.1029/2005JE002512.

Wilhelms, D.E. & McCauley, J.F., 1971. Geologic map of the nearside of the Moon, *U.S. Geological Survey*, I-703.

Williams, K.K. & Zuber, M.T., 1998. Measurement and analysis of lunar basin depths from Clementine altimetry. *Icarus*, 131, 107-122.

Wilson, L. & Head, J.W., III, 2001. Ascent and eruption of mare basalts on the Moon. *Proceedings of 32nd Lunar and Planetary Science Conference*, abstract #1297.

Zhong, S., Parmentier, E.M. & Zuber, M.T., 1999. Early lunar evolution and the origin of asymmetric distribution of mare basalts, *Proceedings of 30th Lunar and Planetary Science Conference*, abstract #1789.

Figure 1. Clementine 750 nm (albedo) image of the Oceanus Procellarum study area, indicating the major geological features of the region. Reiner and Marius craters are marked, as is the Reiner Gamma magnetic anomaly. The white lines are the lava flow boundaries, as mapped by Hiesinger et al. (2003). Two of the lava flows focused on in this work, 'P24' and 'P52', are labelled.

Figure 2. Clementine 750 nm (albedo) image of the Mare Serenitatis study area, indicating the lava flow boundaries and nomenclature of Hiesinger et al. (2000). Dashed lines show two tracks of LRS on *Kaguga* (Ono et al., 2009), results from which are discussed in section 3.2.

Figure 3. Surface TiO_2 wt. % composition (Lucey et al., 2000 algorithm) map for part of the Oceanus Procellarum study area (Figure 1) around lava flow unit 'P52'. Indicated are (i) the thirteen impact craters with TiO_2-poor haloes (labelled 1 to 13) and (ii) additional impact craters in the same unit with no observable halo (labelled 'A' to 'S' and circled with dashed lines).

Figure 4. The mean FeO (according to the algorithm of Wilcox et al., 2005) and TiO_2 (according to the algorithm of Lucey et al., 2000) wt. % contents for the ejecta of the thirteen haloed craters in lava flow unit 'P52', and mean inter-crater values for lava flow 'P52' and 'P24'. Error bars indicate one standard deviation of the individual pixel values used to produce the mean values.

Figure 5. Graphs illustrating that the TiO_2-poor haloes of craters in lava flow unit 'P52' are caused by TiO_2 wt. % content variations rather than surface maturity issues. Data from craters with TiO_2-poor haloes are compared with neighbouring craters without such haloes. (a) 415/750 nm reflectance ratio vs. 750 nm reflectance (albedo) values for the craters in 'P52'; the trend of the two groups is one for increased TiO_2 content rather than increased maturity. (b) mOMAT (according to algorithm of Wilcox et al., 2005) values for both sets of craters; all the craters fall within a narrow range of mature values, there is considerable overlap between the two groups suggesting similar maturity levels. (c) Mean TiO_2 (according to the algorithm of Lucey et al., 2000) wt. % values for the continuous ejecta of the haloed and non-haloed craters as a function of their diameter; there is a clear distinction in terms of TiO_2 abundance between the two groups, with the haloed craters tending to be larger. (d) Albedo of both populations of craters, as a function of their diameter; the range of values for both groups is equal.

734 Figure 6. Maximum excavation depths (in km) for (i) the thirteen impact craters with TiO_2-poor
735 haloes (grey) and (ii) the eighteen craters lacking compositional haloes (black) in lava flow unit
736 'P52'. There is only limited overlap between the values of the two groups (see Figure 5c); this
737 overlap is probably due to underlying topography variations (e.g. buried craters) which cause local
738 variations in the thickness of 'P52'.
739
740 Figure 7. Maps of the Mare Serenitatis study area in terms of (a) FeO (according to the algorithm
741 of Wilcox et al., 2005) and (b) TiO_2 (according to the algorithm of Lucey et al., 2000). The lava
742 flow boundaries and names according to Hiesinger et al. (2000) are shown and the 103 impact
743 craters sampled in this investigation are circled.
744
745 Figure 8. FeO (according to the algorithm of Wilcox et al., 2005) vs. TiO_2 (according to the
746 algorithm of Lucey et al., 2000) wt. % content values for the mean inter-crater areas of the eight
747 lava flow units in the Mare Serenitatis study area. Although the pixels used for sampling the lava
748 flows were chosen at random, an effort was made to avoid any obvious contamination by ejecta
749 rays from distant craters. Error bars represent one standard deviation of the individual pixel values
750 used to determine the mean.
751
752 Figure 9. FeO wt. % (according to the algorithm of Wilcox et al., 2005) vs. TiO_2 wt. % (according
753 to the algorithm of Lucey et al., 2000) compositions for the mean inter-crater areas of the eight
754 lava flow units in the Mare Serenitatis study area (Figure 8). Overlain on these lava flow
755 compositions are: (a) the seven craters in lava flow unit 'S13' that all have a similar composition
756 to the actual unit; (b) twenty-four craters in unit 'S15'. Some of these craters cluster around the
757 composition for the actual unit, however a number of craters plot away from it. Crater 101 is
758 much fresher than the rest of the craters; crater 41 has a composition similar to that of 'S13' and;
759 several craters have more FeO and TiO_2-rich compositions than the flow itself; (c) two craters in
760 unit 'S16'. Crater 102 plots close to the composition of 'S16' whereas crater 103 is more similar
761 to the flow 'S22' with a higher FeO and TiO_2 content; (d) nine craters in unit 'S22'. All the
762 craters cluster around the composition of the unit itself; (e) five craters in unit 'S24'. All these
763 craters cluster close to the composition of the unit itself, however a deeper unit with higher TiO_2
764 content, such as 'S22' may have been excavated and; (f) fifty-six craters in unit 'S28'. Many of
765 the craters cluster close to unit itself, however two deeper units (distributed laterally rather than

766 vertically), one with a lower and one with a higher TiO_2 content seem to have been excavated by
767 two sets of the craters.
768
769 Figure 10. mOMAT (according to the algorithm of Wilcox et al., 2005) values for the 103
770 sampled craters in the Mare Serenitatis study area. All the craters fall within a narrow band of
771 mature values except of the three craters that are labelled; these are fresher, immature craters and
772 are not used in making estimations of lava flow thicknesses.
773
774 Figure 11. Map of the Serenitatis study area with the separate lava flow units and each of the 103
775 impact craters investigated. Circles indicate the sampled impact craters; those which are black
776 have no discernable compositional difference between their ejecta and the lava flow in which they
777 lie; those which appear to have excavated material from a different lithology have been filled with
778 a colour that matches the proposed source. Those in brown have either excavated material from an
779 unidentified deeper lava flow unit with a similar FeO and TiO_2 content to that of 'S22', or whose
780 ejecta are a mixture of the surface lava flow and either 'S11' or 'S18'. The three yellow craters
781 are those which have been identified as fresher than the rest of the population on the basis of their
782 mOMAT values (see Figure 10). The size of the circles is proportional to the diameter (present
783 day rim to rim) of the craters.
784
785 Figure 12. (a) Estimated maximum excavation depths (in metres) of the sampled craters in Mare
786 Serenitatis. Grey numbers are for those craters whose ejecta have originated from a deeper lava
787 flow unit and therefore provide upper bounds for the thickness of the surface lithology (i.e. the
788 surface lava flow must be thinner than the crater's excavation depth). Black numbers are for
789 craters whose ejecta compositions match the lava flow in which they are found and therefore
790 provide lower bounds for the thickness of the surface unit (i.e. the surface lava flow must be
791 thicker than the crater's excavation depth). (b) Surface lava flow unit thickness estimates (in
792 metres) for various points around the study area. These estimates are based on the crater
793 excavation depths shown in (a) and are formulated using crude averages and mid-points. Points A
794 and B are locations cited in Ono et al. (2009) where they state that lava flow unit 'S11' lies at a
795 depth of ~175 m below the surface (at both locations).
796

797 Figure 13. The estimated flux of each of the lava flow units listed in Table 4, as a function of (a)
798 their crater counting age and (b) their mean TiO_2 wt. % content (according to the algorithm of
799 Lucey et al., 2000). Arrows from the data points indicate that the flux values given are likely to be
800 lower limits due to coverage by older lava flows. The shape of the curve in (a) which indicates the
801 change of flux with time (dashed line) compares well with the generalised mare basalt flux model
802 of Head & Wilson (1992) (grey line), especially considering that the actual flux of many of the
803 data points may be considerably higher. The curve shown in (b) illustrates that the flux of the low-
804 Ti basalts is generally higher than that of the high-Ti basalts and therefore the vertical
805 heterogeneity of the mare basalts is similar to that observed purely on the surface. High and low-
806 Ti basalt classification is taken from Neal & Taylor (1992).
807
808 Table 1. List of craters and inter-crater areas for which measurements were obtained in the
809 Oceanus Procellarum study area. Errors listed are 1 σ.
810
811 Table 2. List of craters and inter-crater areas for which measurements were obtained in the Mare
812 Serenitatis study area. Errors listed are 1 σ.
813
814 Table 3. Estimated absolute ages for the lava flow units in the Mare Serenitatis study area. Data
815 are taken from Table 9 of Hiesinger et al. (2000).
816
817 Table 4. Estimated volumes and fluxes for the lava flow units in Oceanus Procellarum (P) and
818 Mare Serenitatis (S) for which thickness estimates have been made. The flow areas and time
819 intervals over which the flows were emplaced are taken from Hiesinger et al. (2000; 2003). The
820 estimated flow thicknesses are established from the spot values shown in Figure 12b.
821
822

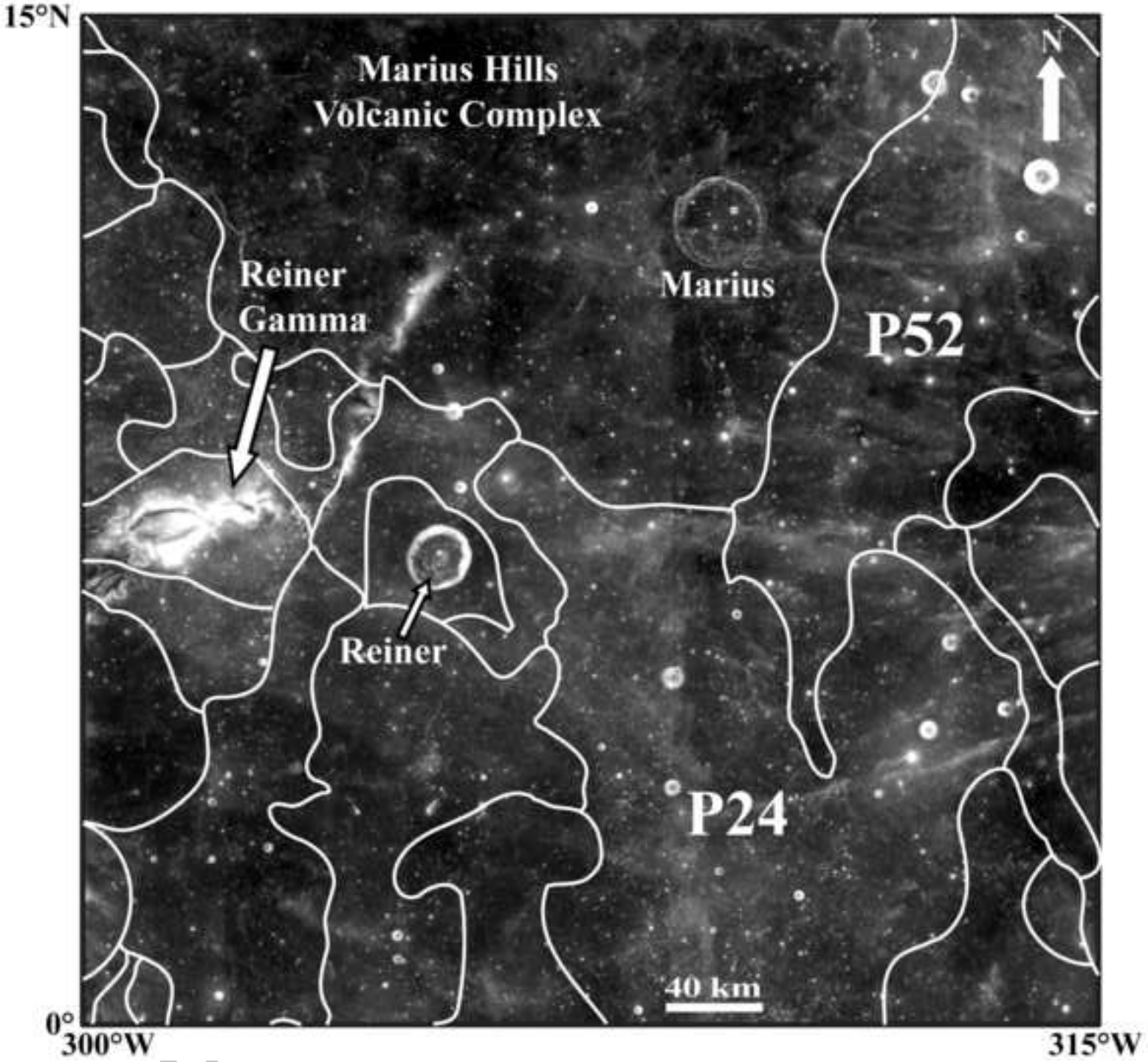

Figure 2

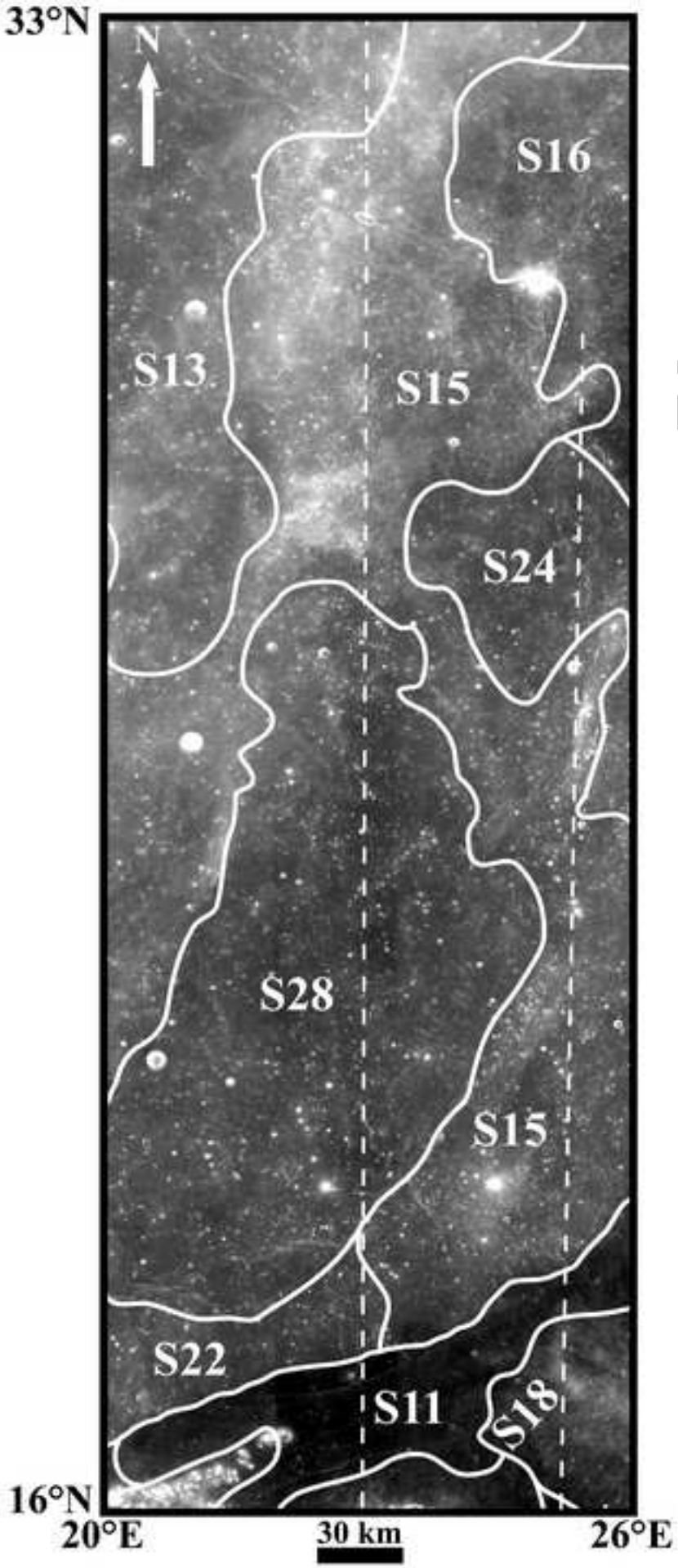

Figure 3

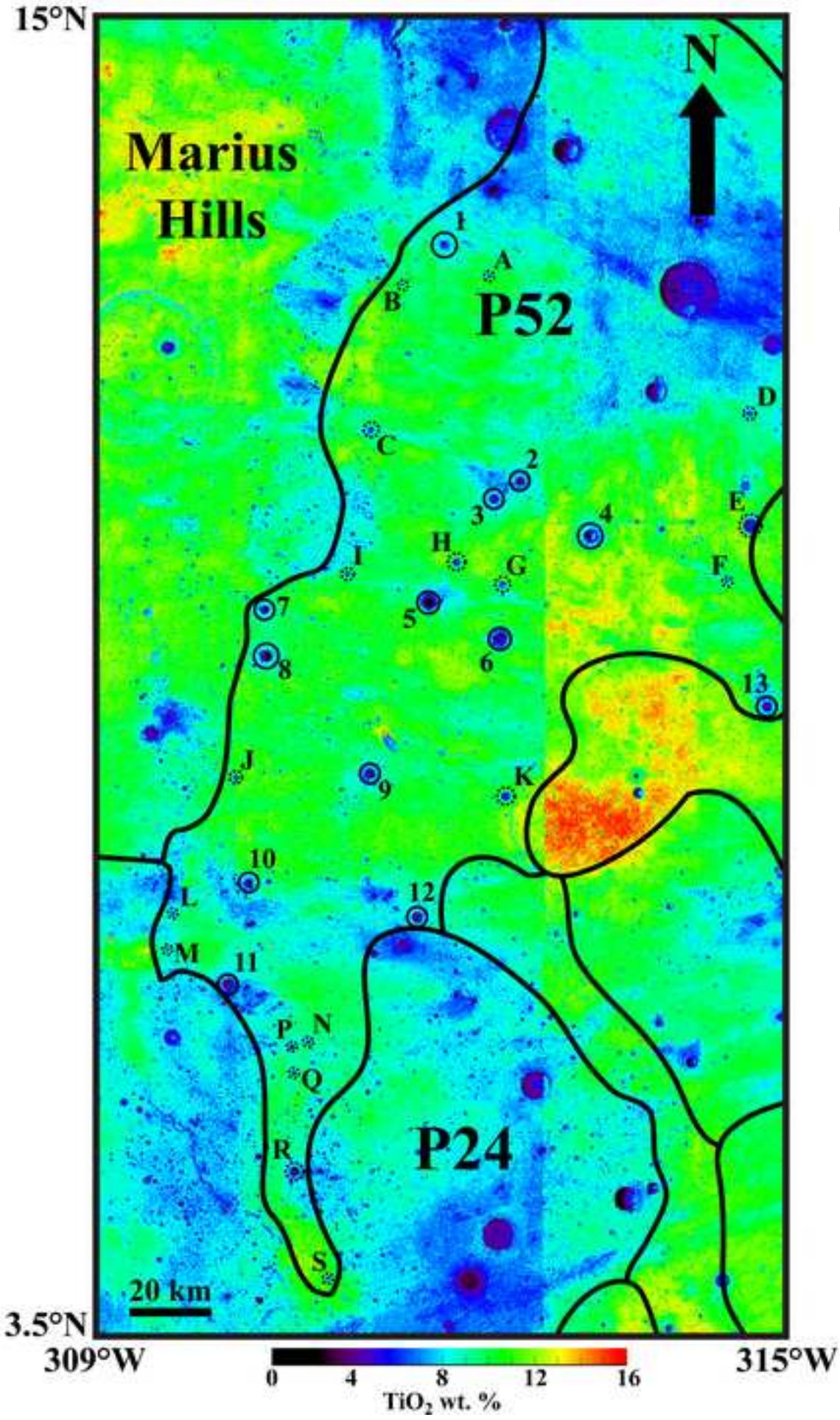

Figure 4

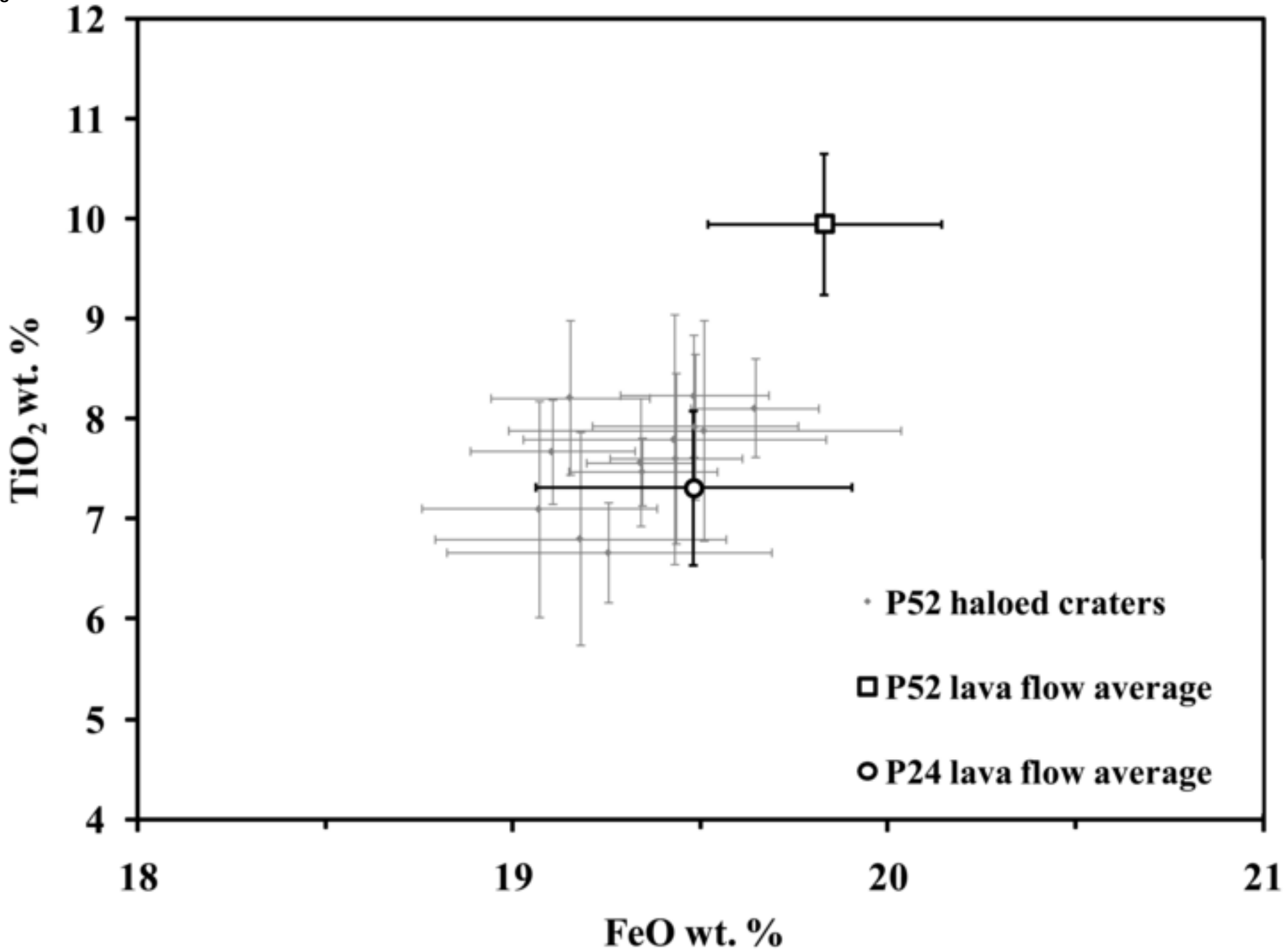

Figure 5

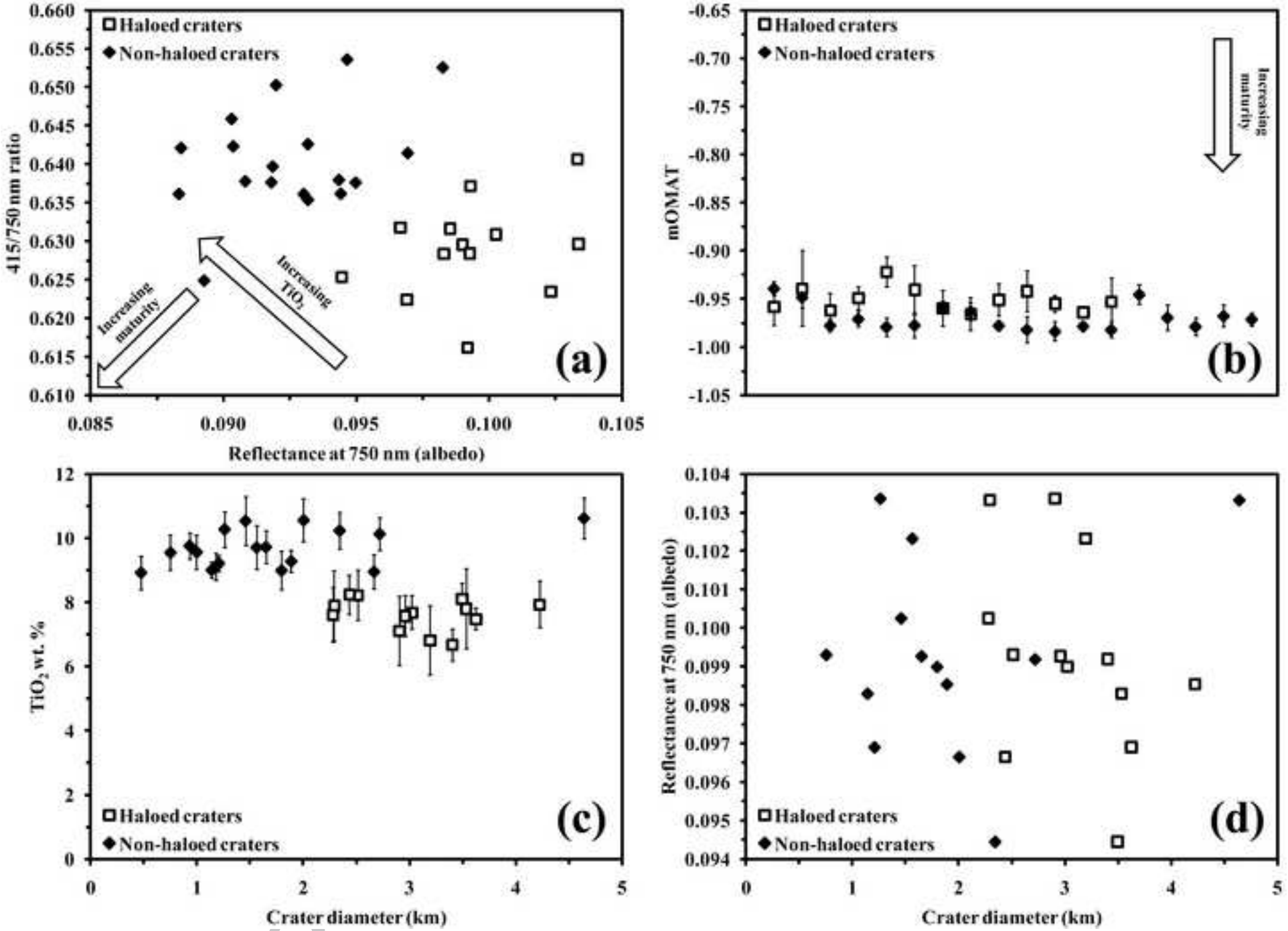

Figure 6

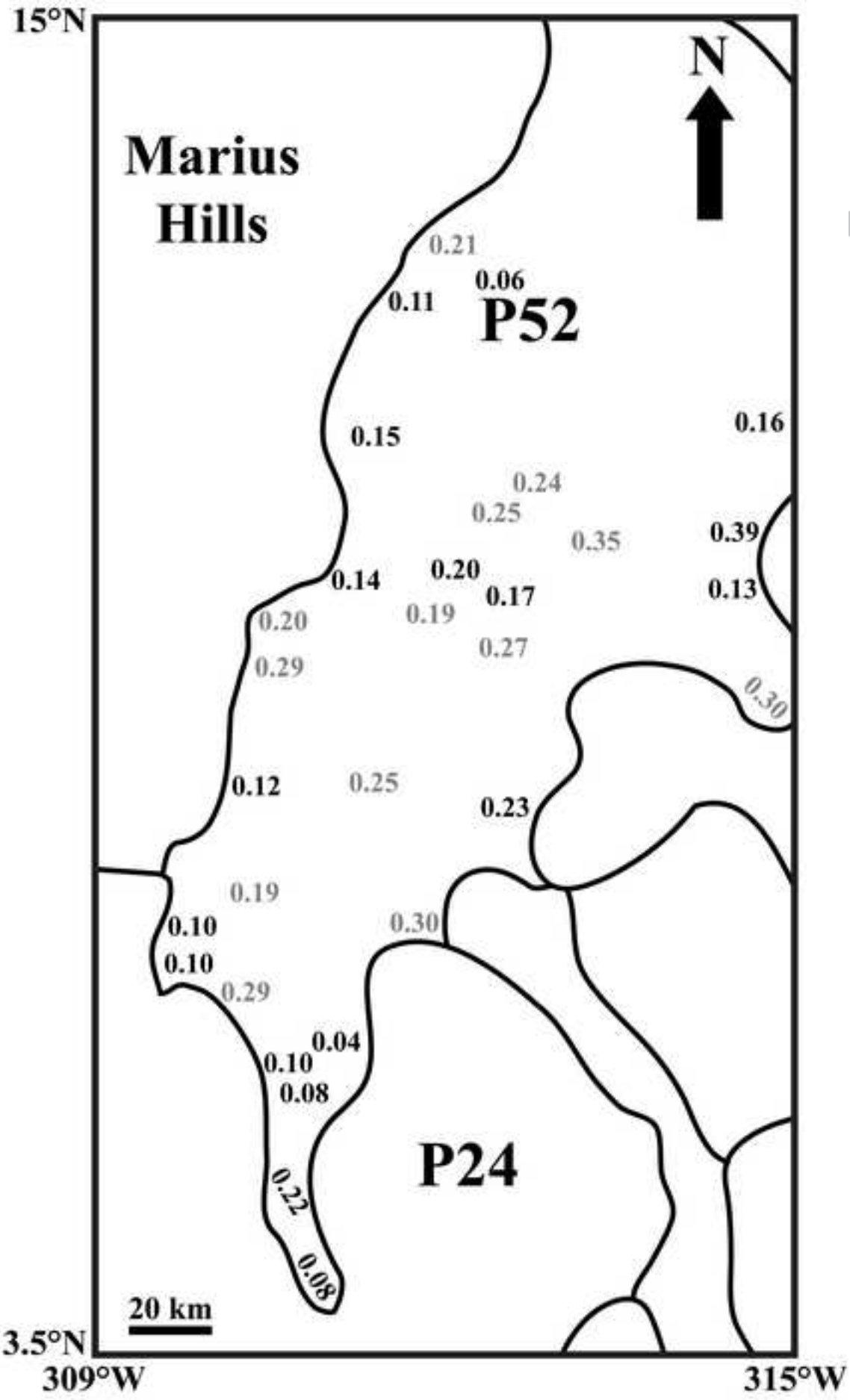

Figure 7

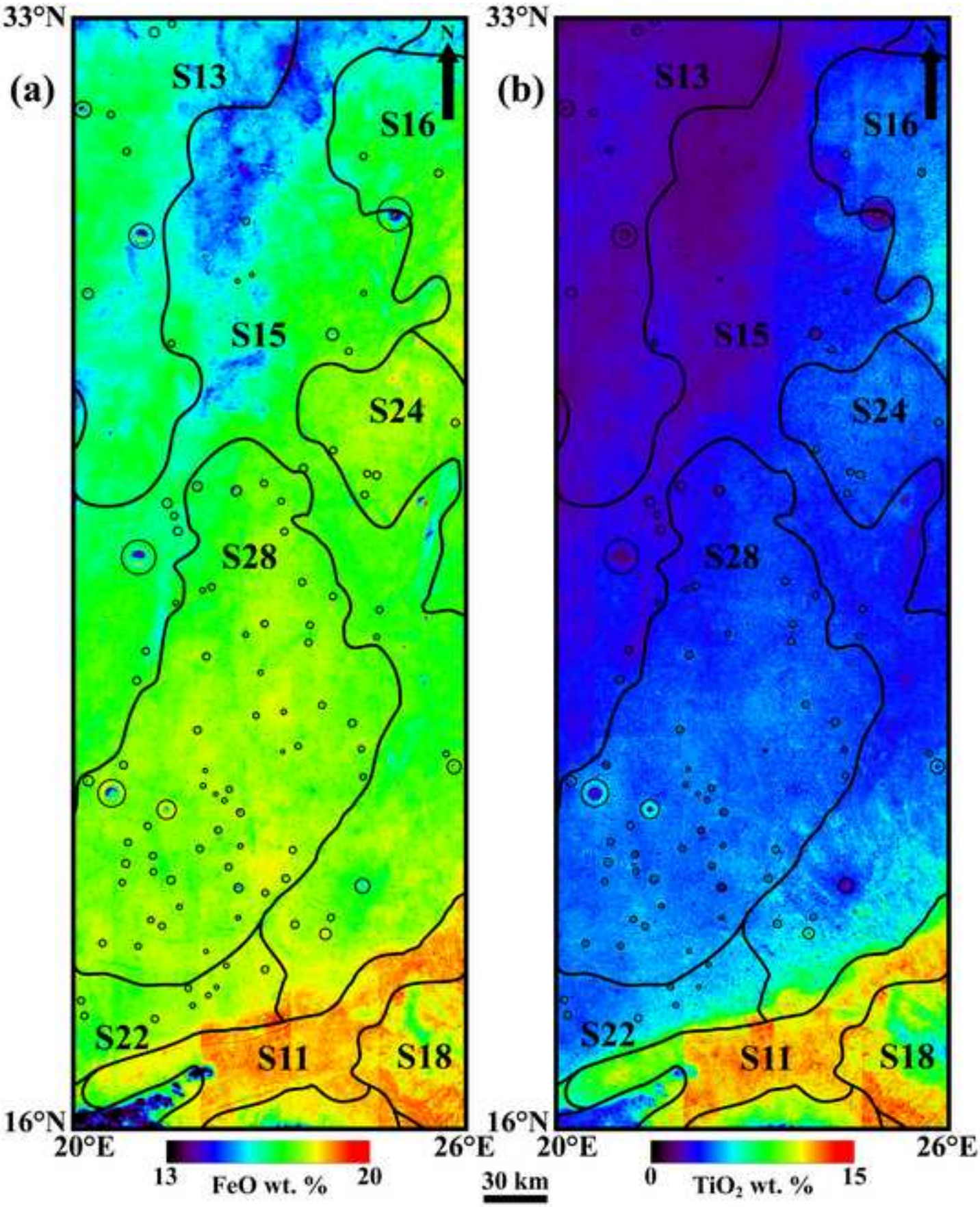

Figure 8

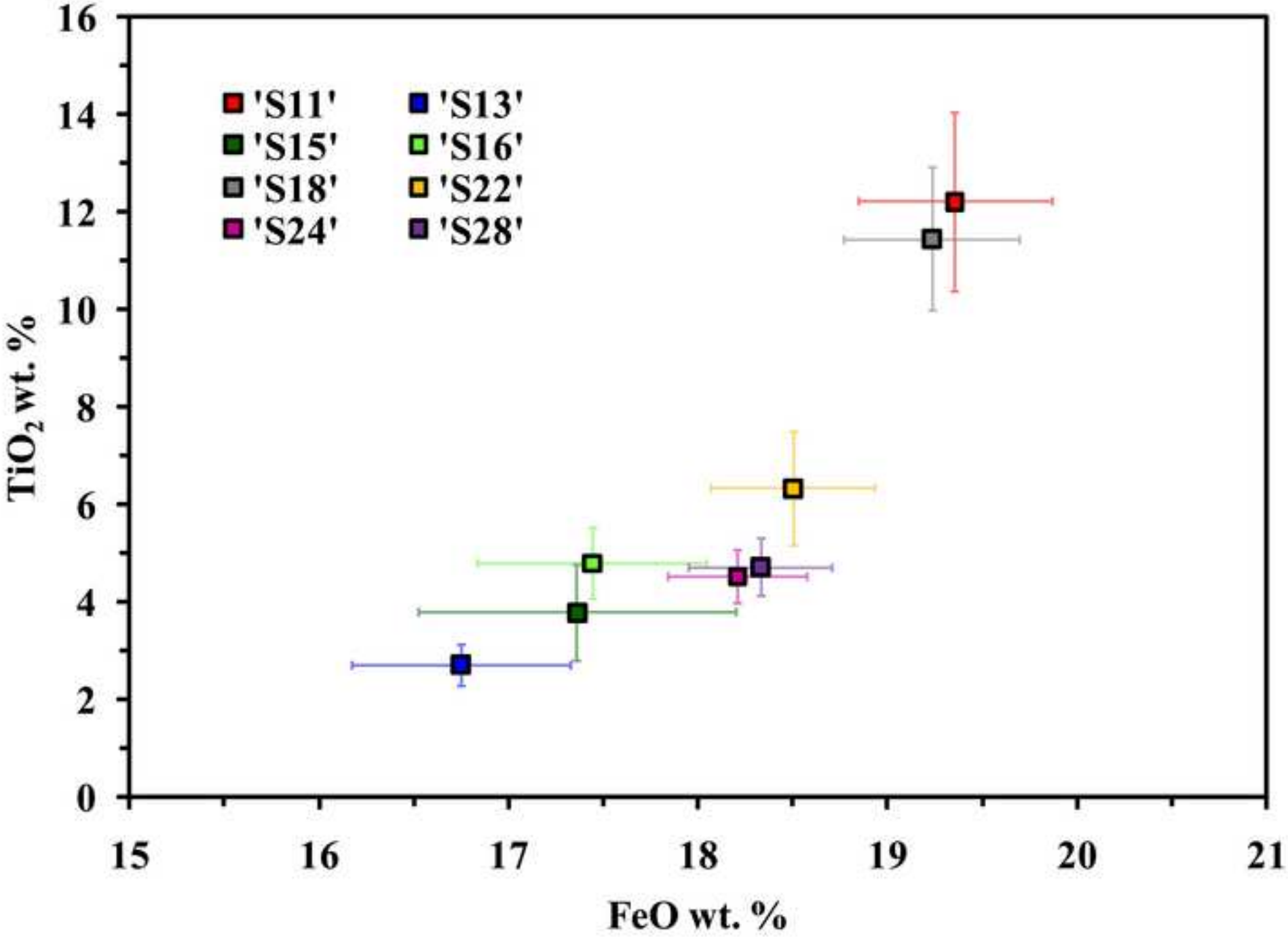
'S11'
'S13'
'S15'
'S16'
'S18'
'S22'
'S24'
'S28'
TiO2 wt. %
FeO wt. %
0
2
4
6
8
10
12
14
16
15
16
17
18
19
20
21

Figure 9

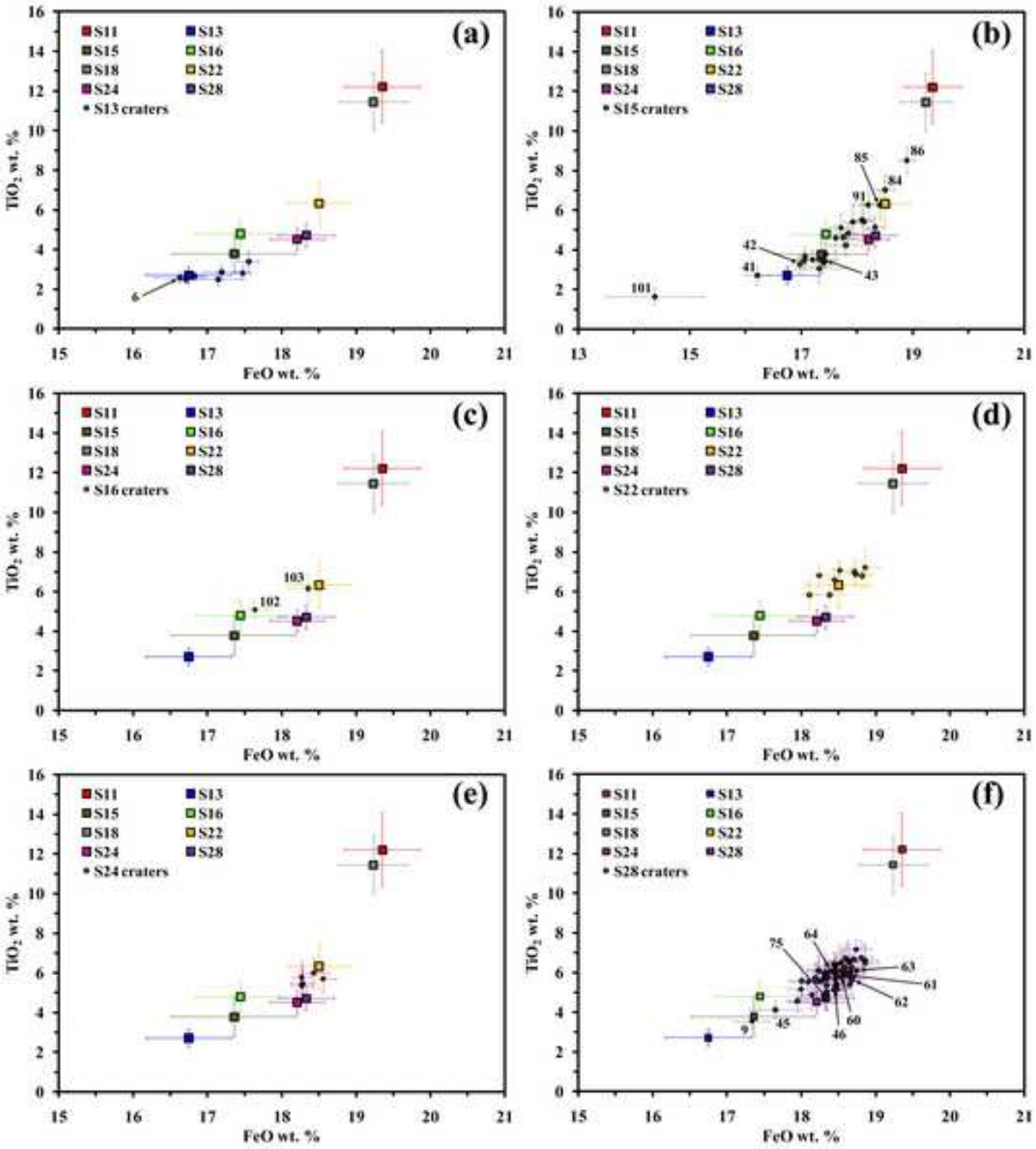

Figure 10

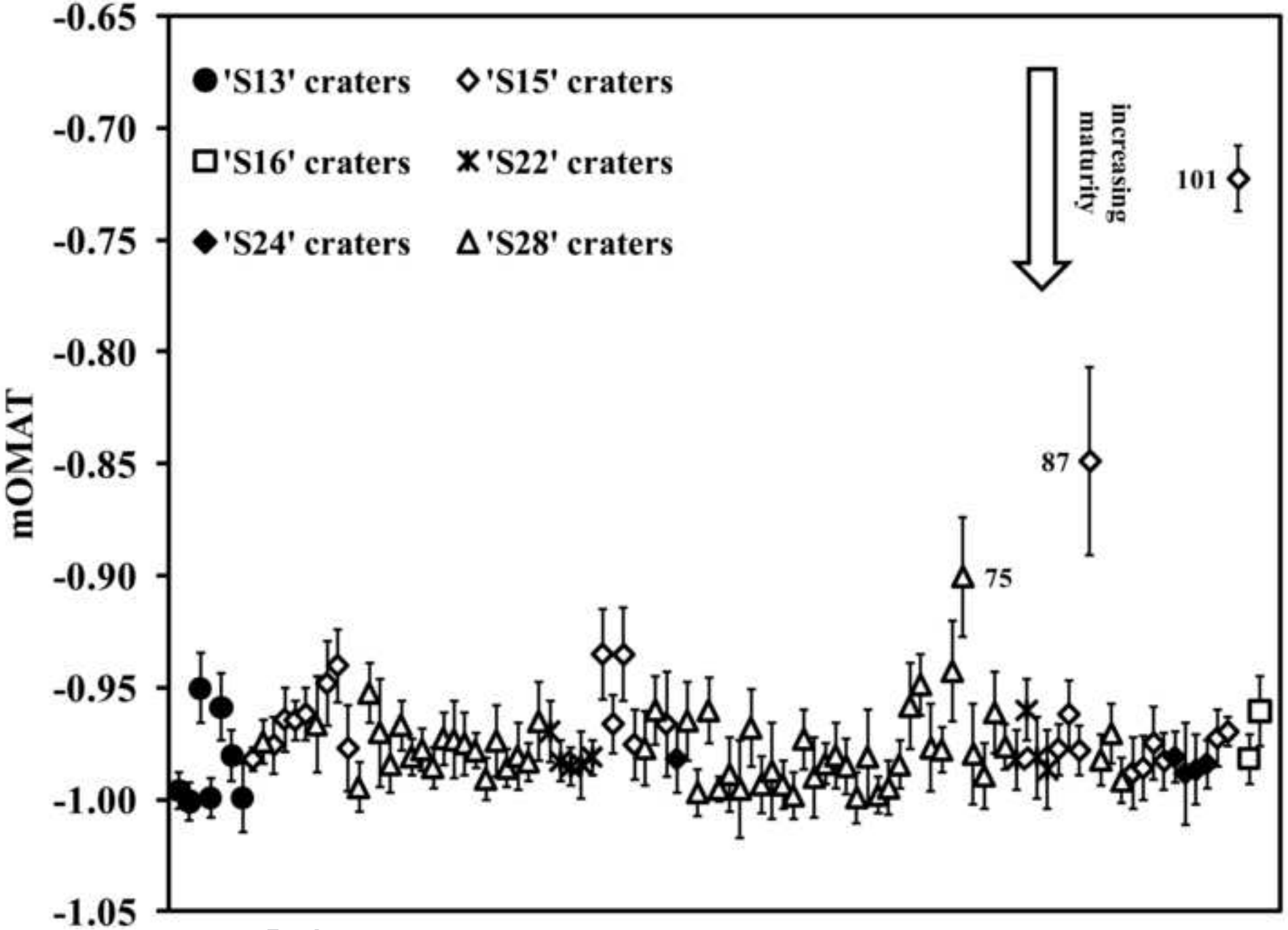

Figure 11

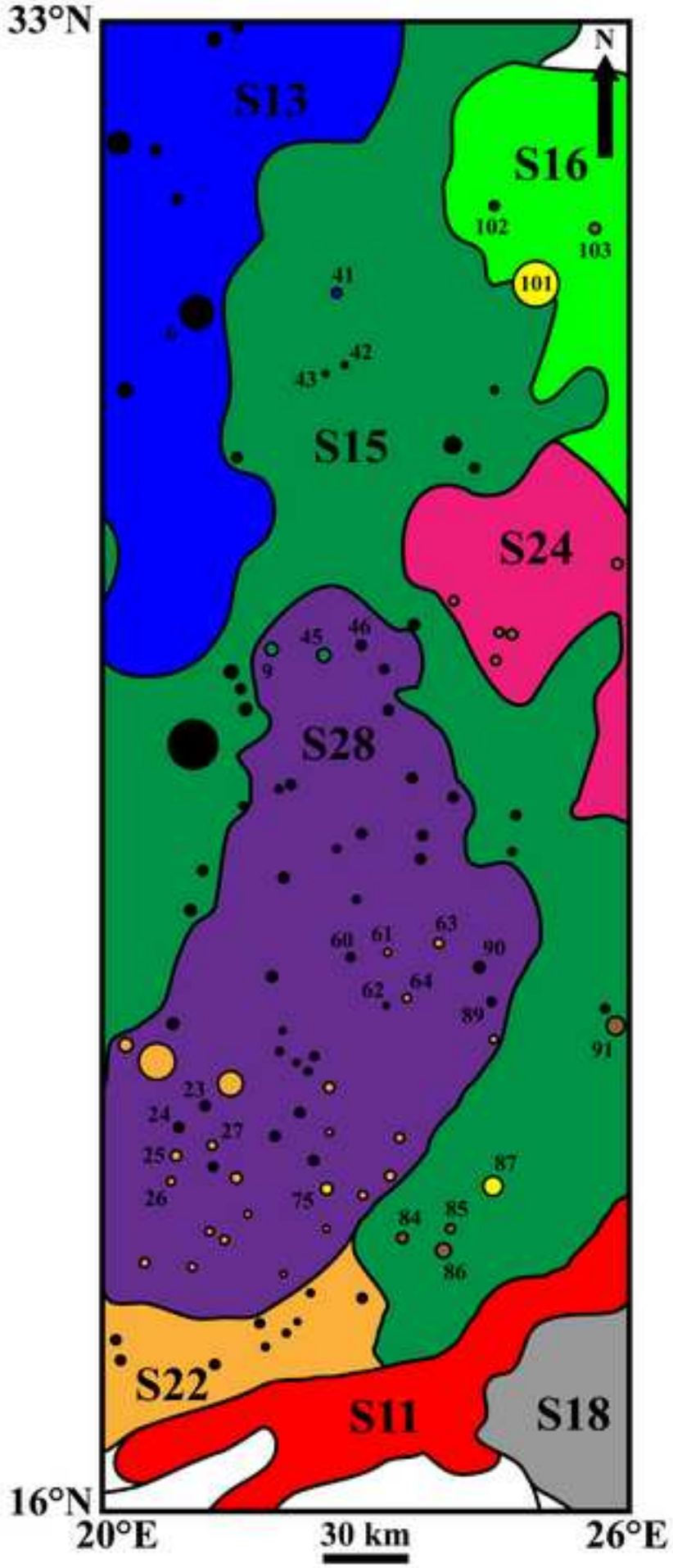

Figure 12

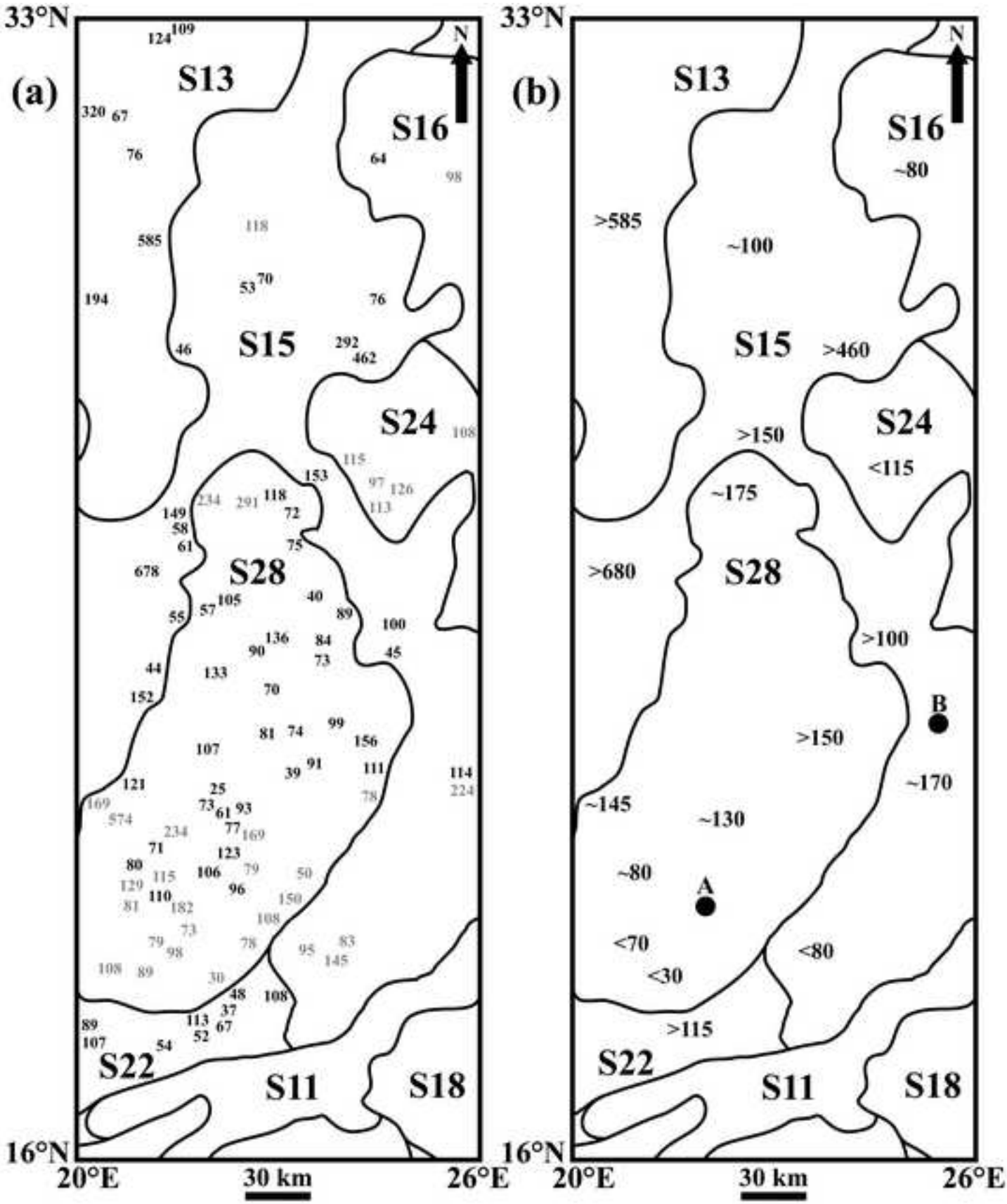

Figure 13

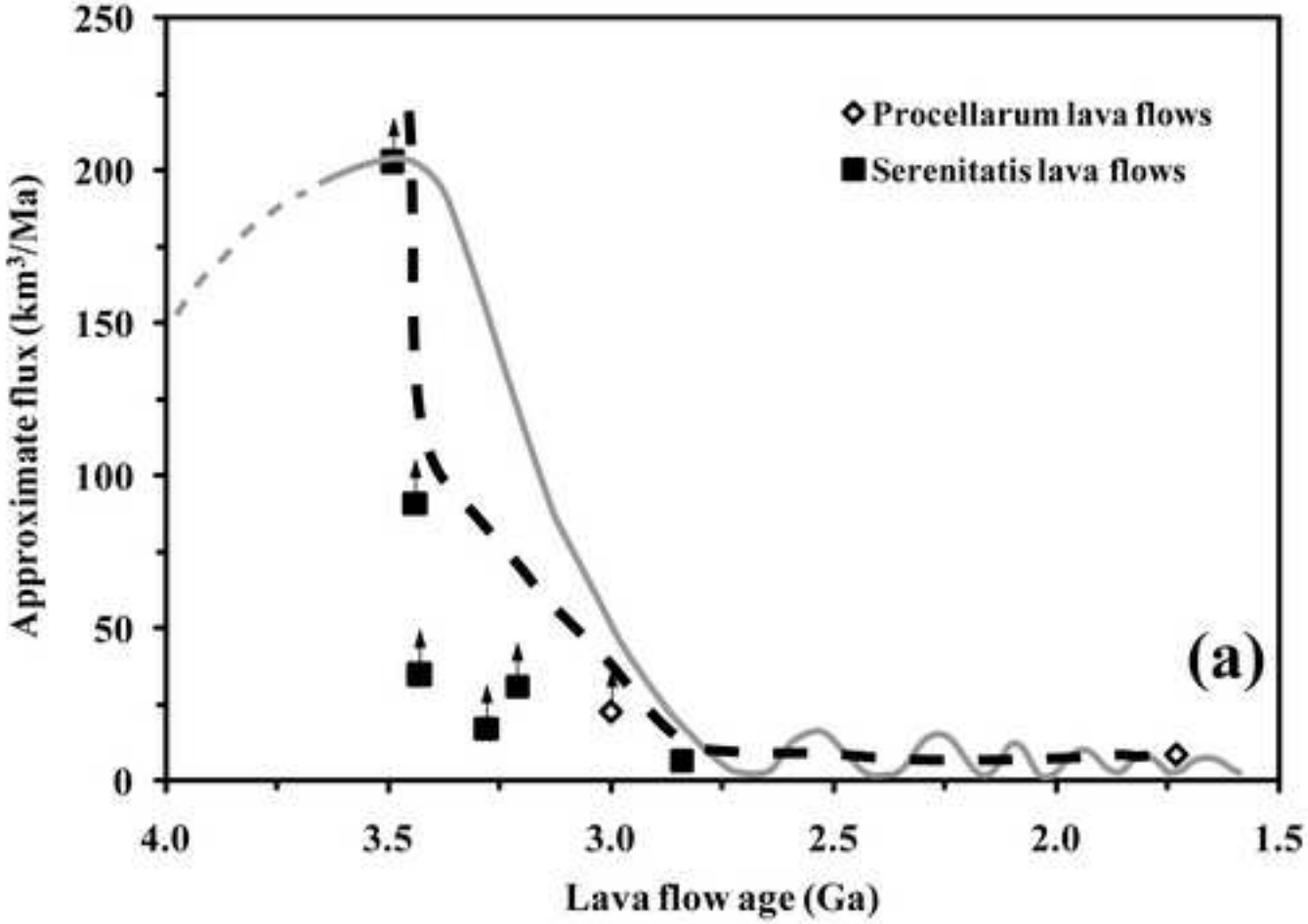

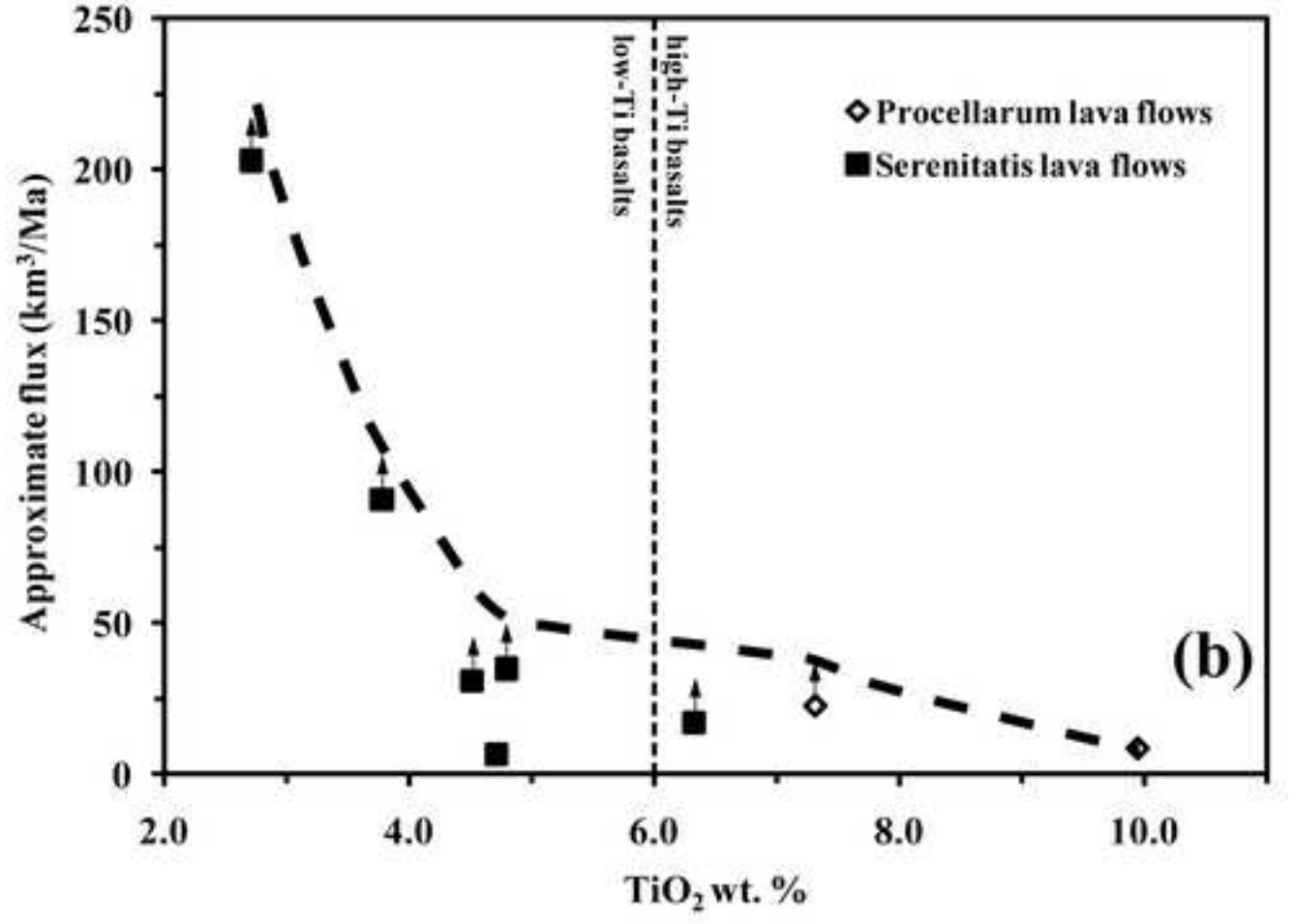

Table 1

Area	Number of pixels sampled	TiO_2 wt. %	mOMAT	Crater diameter (km)	Calculated maximum excavation depth (km)
Crater 1	23	8.22±0.78	-0.96±0.02	2.52	0.21
Crater 2	33	7.10±1.08	-0.94±0.04	2.91	0.24
Crater 3	24	7.68±0.52	-0.96±0.02	3.02	0.25
Crater 4	31	7.92±0.73	-0.95±0.01	4.23	0.35
Crater 5	24	7.88±1.10	-0.92±0.02	2.29	0.19
Crater 6	27	6.81±1.07	-0.94±0.03	3.20	0.27
Crater 7	21	8.23±0.61	-0.96±0.02	2.44	0.20
Crater 8	26	8.11±0.49	-0.97±0.02	3.50	0.29
Crater 9	24	7.57±0.64	-0.95±0.02	3.00	0.25
Crater 10	21	7.61±0.86	-0.94±0.02	2.28	0.19
Crater 11	35	6.67±0.50	-0.96±0.01	3.40	0.29
Crater 12	27	7.47±0.34	-0.96±0.01	3.63	0.30
Crater 13	23	7.80±1.25	-0.95±0.02	3.53	0.30
Crater A	10	9.54±0.55	-0.94±0.01	0.75	0.06
Crater B	10	10.27±0.56	-0.95±0.01	1.26	0.11
Crater C	10	8.98±0.60	-0.98±0.01	1.80	0.15
Crater D	15	9.27±0.34	-0.97±0.01	1.89	0.16
Crater E	18	10.61±0.64	-0.98±0.01	4.65	0.39
Crater F	7	9.70±0.68	-0.98±0.01	1.56	0.13
Crater G	10	10.55±0.67	-0.96±0.01	2.01	0.17
Crater H	13	10.22±0.57	-0.96±0.01	2.35	0.20
Crater I	11	9.71±0.50	$-0.98\pm4\times10^{-3}$	1.65	0.14
Crater J	11	10.53±1.46	-0.98±0.01	1.46	0.12
Crater K	20	10.12±0.50	-0.98±0.01	2.72	0.23
Crater L	9	9.20±0.25	$-0.98\pm4\times10^{-3}$	1.21	0.10
Crater M	9	9.00±0.25	-0.98±0.01	1.14	0.10
Crater N	8	8.91±0.52	-0.95±0.01	0.48	0.04
Crater P	7	9.10±0.42	-0.97±0.01	1.18	0.10
Crater Q	11	9.55±0.53	-0.98±0.01	1.00	0.08
Crater R	18	8.94±0.52	-0.97±0.01	2.67	0.22
Crater S	11	9.75±0.41	-0.97±0.01	0.93	0.08
‘P24’ inter-crater area	109	7.31±0.77	-0.97±0.02	-	-
‘P52’ inter-crater area	236	9.95±0.70	-0.97±0.01	-	-

Table 2

Lava flow / crater	No. pixels sampled	Crater found in lava flow	TiO_2 wt. %	mOMAT	Crater diameter (km)	Max. exc. depth (m)
S11	170	-	12.21±1.83	-1.02±0.02	-	-
S13	169	-	2.71±0.43	-0.99±0.01	-	-
S15	497	-	3.78±0.98	-0.98±0.01	-	-
S16	121	-	4.79±0.73	-0.99±0.02	-	-
S18	62	-	11.44±1.46	-0.98±0.01	-	-
S22	69	-	6.33±1.16	-1.00±0.01	-	-
S24	132	-	4.52±0.56	-0.98±0.01	-	-
S28	262	-	4.71±0.60	-0.99±0.01	-	-
Crater 1	21	S13	2.67±0.21	-1.00±0.01	1.29	109
Crater 2	31	S13	2.50±0.21	-1.00±0.01	1.47	124
Crater 3	32	S13	2.50±0.34	-0.95±0.02	3.81	320
Crater 4	17	S13	2.82±0.33	-1.00±0.01	0.80	67
Crater 5	22	S13	3.40±0.54	-0.96±0.01	0.91	76
Crater 6	31	S13	2.59±0.28	-0.98±0.01	6.97	585
Crater 7	34	S13	2.87±0.32	-1.00±0.02	2.31	194
Crater 8	17	S15	3.36±0.22	-0.98±0.01	0.55	46
Crater 9	30	S28	3.55±0.38	-0.97±0.01	2.78	234
Crater 10	17	S15	3.46±0.45	-0.98±0.01	1.77	149
Crater 11	20	S15	3.52±0.43	-0.96±0.01	0.69	58
Crater 12	18	S15	3.68±0.45	-0.96±0.01	0.72	61
Crater 13	55	S15	3.52±0.39	-0.96±0.01	8.07	678
Crater 14	18	S28	4.55±0.58	-0.97±0.02	0.68	57
Crater 15	22	S15	4.63±0.43	-0.95±0.02	0.65	55
Crater 16	22	S15	3.79±0.60	-0.94±0.02	0.53	44
Crater 17	28	S15	5.11±0.67	-0.98±0.02	1.81	152
Crater 18	35	S28	6.06±0.92	-0.99±0.01	1.28	107
Crater 19	24	S28	5.40±0.44	-0.95±0.01	1.44	121
Crater 20	37	S28	5.56±0.76	-0.97±0.02	2.01	169
Crater 21	74	S28	6.50±0.64	-0.98±0.01	6.84	574
Crater 22	56	S28	7.17±0.47	-0.97±0.01	2.78	234
Crater 23	26	S28	6.00±0.59	-0.98±0.01	0.84	71
Crater 24	22	S28	5.74±0.46	-0.98±0.01	0.96	80
Crater 25	31	S28	6.39±0.65	-0.99±0.01	1.54	129
Crater 26	25	S28	6.28±0.59	-0.97±0.01	0.96	81
Crater 27	24	S28	6.12±0.74	-0.97±0.02	1.37	115
Crater 28	25	S28	5.77±0.80	-0.98±0.01	1.26	106
Crater 29	26	S28	5.96±0.75	-0.98±0.01	1.31	110
Crater 30	33	S28	6.11±0.70	-0.99±0.01	2.16	182
Crater 31	22	S28	6.40±0.57	-0.97±0.02	0.87	73
Crater 32	24	S28	6.73±0.69	-0.99±0.01	0.94	79
Crater 33	25	S28	6.67±0.51	-0.98±0.01	1.17	98
Crater 34	25	S28	6.24±0.75	-0.98±0.08	1.07	89

Crater 35	24	S28	6.48±0.86	-0.97±0.02	1.29	108
Crater 36	24	S22	5.83±0.90	-0.97±0.01	1.06	89
Crater 37	23	S22	5.83±0.70	-0.98±0.01	1.27	107
Crater 38	18	S22	7.07±0.46	-0.99±0.01	0.65	54
Crater 39	25	S22	6.81±0.60	-0.98±0.02	1.35	113
Crater 40	21	S22	6.59±0.59	-0.98±0.01	0.62	52
Crater 41	30	S15	2.71±0.49	-0.94±0.02	1.41	118
Crater 42	15	S15	3.26±0.47	-0.97±0.01	0.83	70
Crater 43	20	S15	3.42±0.35	-0.94±0.02	0.63	53
Crater 44	63	S15	4.23±0.52	-0.98±0.02	3.47	292
Crater 45	44	S28	4.13±0.45	-0.98±0.02	3.46	291
Crater 46	26	S28	5.12±0.71	-0.96±0.02	1.41	118
Crater 47	30	S15	5.51±0.75	-0.97±0.02	1.82	153
Crater 48	31	S24	5.77±0.81	-0.98±0.02	1.37	115
Crater 49	22	S28	5.02±0.92	-0.96±0.02	0.86	72
Crater 50	24	S28	5.16±0.69	-1.00±0.01	0.89	75
Crater 51	23	S28	4.89±0.79	-0.96±0.01	1.25	105
Crater 52	15	S28	5.36±0.53	-0.96±0.01	0.48	40
Crater 53	18	S28	5.16±0.57	-0.99±0.02	1.06	89
Crater 54	26	S28	5.67±0.75	-1.00±0.02	1.61	136
Crater 55	24	S28	5.75±0.74	-0.97±0.02	1.00	84
Crater 56	26	S28	5.52±0.61	-0.99±0.01	1.07	90
Crater 57	30	S28	5.58±0.92	-0.99±0.02	1.58	133
Crater 58	24	S28	5.69±0.66	-0.99±0.01	0.87	73
Crater 59	22	S28	5.31±0.67	-1.00±0.01	0.83	70
Crater 60	27	S28	5.87±0.76	-0.97±0.01	0.97	81
Crater 61	23	S28	6.00±0.76	-0.99±0.02	0.89	74
Crater 62	18	S28	5.64±0.79	-0.98±0.01	0.46	39
Crater 63	30	S28	6.24±0.71	-0.98±0.01	1.18	99
Crater 64	25	S28	6.07±0.60	-0.99±0.01	1.08	91
Crater 65	18	S28	5.97±0.67	-1.00±0.01	0.29	25
Crater 66	22	S28	5.92±1.02	-0.98±0.02	1.11	93
Crater 67	18	S28	5.78±0.72	-1.00±0.01	0.87	73
Crater 68	15	S28	6.00±0.61	-0.99±0.01	0.72	61
Crater 69	21	S28	5.96±0.71	-0.98±0.01	0.92	77
Crater 70	46	S28	6.09±0.55	-0.96±0.02	2.01	169
Crater 71	32	S28	5.41±0.52	-0.95±0.01	1.47	123
Crater 72	27	S28	6.05±0.59	-0.98±0.02	0.94	79
Crater 73	20	S28	6.76±0.79	-0.98±0.01	0.60	50
Crater 74	31	S28	5.82±0.63	-0.94±0.02	1.15	96
Crater 75	40	S28	4.82±0.74	-0.90±0.03	1.47	123
Crater 76	26	S28	6.55±0.87	-0.98±0.02	1.79	150
Crater 77	33	S28	6.25±0.97	-0.99±0.01	1.29	108
Crater 78	24	S28	6.58±1.01	-0.96±0.02	0.93	78

Crater 79	16	S28	6.61±0.85	-0.98±0.01	0.35	30
Crater 80	27	S22	6.80±0.76	-0.98±0.01	0.57	48
Crater 81	24	S22	7.21±0.99	-0.96±0.01	1.29	108
Crater 82	18	S22	6.88±0.69	-0.98±0.02	0.44	37
Crater 83	22	S22	7.00±0.64	-0.99±0.02	0.79	67
Crater 84	38	S15	7.02±0.72	-0.98±0.01	1.13	95
Crater 85	35	S15	6.27±0.74	-0.96±0.02	0.99	83
Crater 86	28	S15	8.52±0.67	-0.98±0.01	1.73	145
Crater 87	66	S15	3.06±0.75	-0.85±0.04	1.29	109
Crater 88	22	S28	5.59±0.73	-0.98±0.01	0.93	78
Crater 89	30	S28	5.74±0.87	-0.97±0.01	1.32	111
Crater 90	30	S28	5.72±0.76	-0.99±0.01	1.85	156
Crater 91	42	S15	6.26±0.78	-0.99±0.02	2.66	224
Crater 92	26	S15	5.40±0.86	-0.99±0.01	1.36	114
Crater 93	21	S15	5.42±0.93	-0.97±0.02	0.54	45
Crater 94	22	S15	4.61±0.66	-0.98±0.01	1.19	100
Crater 95	31	S24	5.36±0.79	-0.98±0.01	1.34	113
Crater 96	24	S24	5.47±0.90	-0.99±0.02	1.16	97
Crater 97	28	S24	5.99±0.72	-0.99±0.02	1.50	126
Crater 98	23	S24	5.70±0.75	-0.98±0.01	1.29	108
Crater 99	19	S15	5.13±0.55	-0.97±0.01	0.55	462
Crater 100	13	S15	4.84±0.50	-0.97±0.01	0.91	76
Crater 101	30	S15	1.64±0.40	-0.72±0.01	2.26	190
Crater 102	17	S16	5.09±0.44	-0.98±0.01	0.76	64
Crater 103	27	S16	6.15±0.73	-0.96±0.02	1.17	98

Table 3

Lava flow unit	Model age (Ga)	Error (Ga)
S28	2.84	+0.16 / -0.18
S24	3.21	+0.07 / -0.09
S22	3.28	+0.09 / -0.17
S18	3.42	+0.10 / -0.08
S16	3.43	+0.09 / -0.09
S15	3.44	+0.03 / -0.06
S13	3.49	+0.08 / -0.05
S11	3.55	+0.05 / -0.09

Table 4

Lava flow unit	Estimated average thickness (km)	Surface area (km^2)	Approximate volume (km^3)	Maximum interval of emplacement (Ma)	Approximate average flux (km^3/Ma)
'P24'	0.25	6300	1575	70	22.5
'P52'	0.25	4075	1020	120	8.5
'S13'	0.6	10173	6100	30	203
'S15'	0.5	9089	4545	50	91
'S16'	0.08	4363	350	10	35
'S22'	0.1	3415	340	20	17
'S24'	0.1	6201	620	20	31
'S28'	0.1	3927	390	60	6.5